Preprint version of a paper published by Elsevier in Tribology International Volume XXX, Accepted on 27 April 2026,
https://doi.org/10.1016/j.triboint.2026.112118

Next-gen hybrid greases: Ionic liquids and nickel-functionalised carbon nanotubes in metal-polymer lubrication

Ł. Wojciechowski* [a], J. Kałużny [b], **K.J. Kubiak** [c], S. Boncel [d] [e] [f], M. Skrzypek [a], T. Runka [g], B. Gapiński [h], A.A. Marek [d] [e] [i], S. Ruczka [d] [e], T.G. Mathia [j]

[a] Institute of Machines and Motor Vehicles (IMRiPS), Poznan University of Technology, Poland
[b] Institute of Powertrains & Aviation, Poznan University of Technology, Poland
[c] School of Mechanical Engineering, University of Leeds, United Kingdom
[d] Centre for Organic and Nanohybrid Electronics, Silesian University of Technology (CONE), Poland
[e] Department of Organic Chemistry, Bioorganic Chemistry and Biotechnology, Silesian University of Technology, Poland
[f] NanoCarbonGroup.com Co. Ltd., Poland
[g] Institute of Materials Research and Quantum Engineering, Poznan University of Technology, Poland
[h] Division of Metrology & Measurement Systems, Poznan University of Technology, Poland
[i] Department of Chemical Organic Technology and Petrochemistry, Silesian University of Technology, Poland
[j] Laboratoire de Tribologie et Dynamique des Systèmes – C.N.R.S., École Centrale de Lyon, France

Abstract

This study explores a new approach to hybrid lubrication by combining an ionic liquid with nickel-decorated carbon nanotubes. The aim was to develop a grease capable of merging the chemical activity of the ionic liquid with the tribochemical adaptability of the nanocarbon phase. TEM/EDX analyses confirmed an efficiency of the nickel decoration, resulting in locally wrapped nanotube clusters that may influence interfacial reactivity. Friction tests performed for polyamide-6 (PA) and ultra-high molecular weight polyethylene (UHMWPE) sliding, as polar and non-polar polymers, respectively, against AISI 4130 steel showed a marked reduction in friction for all ionic-liquid-based lubricants compared with a commercial reference polyurea grease. For PA, the synergy between the ionic liquid and Ni-CNTs produced the lowest and most stable friction, attributed to the exfoliation of CNTs into quasi-graphene lamellae that formed shear-adaptive tribofilms. In UHMWPE, the neat ionic liquid provided the best frictional response, as CNTs remained embedded within the transfer layer and did not participate in lamellar film formation. Overall, the results demonstrate that ionic-liquid- and nanocarbon-based hybrid greases can be tuned to promote either chemical or lamellar lubrication pathways, depending on the mechanical response of the polymer.

Nomenclature:	
AFC	Abbott-Firestone curve
CNT(s)	Carbon nanotube(s)
COF	Coefficient of friction
EDS	Energy Dispersive Spectroscopy
IL(s)	Ionic liquid(s)
NC(s)	Nanocarbon(s)
SEM	Scanning Electron Microscopy
SFE	Surface free energy
TEM	Transmission Electron Microscopy
Vmc	Core material volume [ml/m^2]
Vmp	Peak material volume [ml/m^2]
Vvc	Core void volume [ml/m^2]
Vvv	Valley void volume [ml/m^2]

1. Introduction

The current development of tribology aligns with global efforts to drive the next technological breakthroughs. These challenges include, among others, the transformation of propulsion systems in the automotive industry (and in the future, potentially

*Corresponding author: Lukasz Wojciechowski, Institute of Machines and Motor Vehicles, Poznan University of Technology, ul. Piotrowo 3, 60-965 Poznan, Poland, e-mail: Lukasz.Wojciechowski@put.poznan.pl

in aviation), the advancement of crewed space exploration, the gradual elimination of fossil-based components in lubricant formulations, and the implementation of more effective waste management systems addressing the environmental impact of modern civilization.

Such changes create specific demands for tribological systems. Reducing friction in kinematic pairs remains a key challenge, with the ultimate aspiration of reaching superlubricity and nearly eliminating wear [1]. Over the past decade, superlubricity has received increasing attention due to its extraordinary potential to significantly lower energy dissipation in sliding contacts [2-3]. In tribological terms, superlubricity refers to a distinct lubrication regime where the friction between interacting surfaces is extremely low – approaching near-frictionless conditions, and is conventionally defined by a coefficient of friction (COF) below 0.01 [4-6]. Superlubricity can generally be divided into two main categories: solid and liquid, depending on the medium and the physical mechanism responsible for the drastic reduction of friction. In the case of solid (structural) superlubricity, the decisive factor is the incommensurability of the contacting crystalline surfaces. When the atomic lattices of two solids cannot achieve perfect registry, the corrugation of the interfacial potential energy landscape is effectively suppressed. As a result, interatomic forces partially cancel out, which markedly reduces the resistance to sliding and enables the attainment of the superlubricity effect [5,7-8]. Three- and two-dimensional layered materials, most notably graphite [9-11], graphene [12-13], and hexagonal boron nitride [14], have provided well-established examples of solid superlubricity. In addition, ultralow-friction states consistent with superlubricity have also been reported in disordered carbon-based coatings such as diamond-like carbon (DLC) films [15-18] and in lamellar transition-metal dichalcogenides, *e.g.*, molybdenum disulphide (MoS_2) [19-20].

In contrast, liquid superlubricity arises when suitable lubricating liquids form ultrathin films with extremely low shear resistance between sliding surfaces. Examples include aqueous solutions containing glycerol [21-23], acids [24-26], or ionic liquids (ILs) [27-30], which can induce the formation of an ordered boundary layer that facilitates nearly frictionless motion. This effect can be further enhanced by various additives (including nanoscale ones), whose action may both improve the durability of the formed boundary layers and promote synergistic protective mechanisms (liquid phase + additive) at the interface. Noteworthy examples of nanoadditives that have demonstrated macroscopic performance levels potentially suitable for practical applications include layered double hydroxides (LDHs) dispersed in IL–alcohol solutions [31], black phosphorus nanosheets incorporated into water-based lubricants [32], and copper nanoparticles suspended in glycerol [33]. It appears, however, that carbon-based nanostructures constitute the group of additives most frequently employed and most comprehensively studied in the context of superlubricity. This predominance is largely due to their unique structural versatility and proven ability to interact synergistically with lubricating liquids. In particular, graphene derivatives [34] and carbon nanotubes (CNTs) [35-36] are the most widely applied representatives of this class, which have been extensively investigated for their ability to promote ultralow friction states. Nevertheless, it should be emphasised that extensive investigation does not necessarily imply a complete or unequivocal understanding of their underlying mechanisms of action.

The ability of graphene and its derivatives to reduce friction and wear is associated with the formation of incommensurate interfaces, as discussed earlier. In this context, the key mechanism is the interaction of graphene sheets or flakes that slide over one another with ultralow friction within the interfacial region of the contacting surfaces. The liquid lubricant phase serves as a carrier, while the homogeneous dispersion of graphene is of critical importance [37-38]. In the case of graphene, additional factors are also highlighted that contribute to the improved lubricating performance of liquid formulations in which it is incorporated as an additive. Particular attention is paid to enhancing thermal conductivity [39-40] and the resulting dissipation of heat from the contact, forming an oxidation barrier that slows down lubricant degradation [41], and a so-called healing effect, whereby graphene sheets fill micro-damages and thereby prevent their further propagation [42].

CNTs represent the second most widely employed class of carbon nanostructures in the context of their anti-friction and anti-wear functionality. Their unique physicochemical characteristics, including a pronounced tendency to agglomerate, mean that their tribological behaviour can exert either beneficial or detrimental effects on the durability of the tribological pair. There are numerous reports attributing the antifriction effect of CNTs to the so-called rolling bearing mechanism [43-46], according to which spherical or circular-section nanoparticles can transform sliding friction into rolling motion, analogous to the operation of rolling bearings. However, this effect appears to be attainable primarily under idealised conditions, involving simplified smooth surfaces and high chemical homogeneity [47]. In contrast, real engineering applications, all these factors raise questions about the feasibility of genuine bearing-like behaviour of CNTs under the operating conditions of practical tribological contacts. In addition, due to their geometry (microscale length combined with nanoscale diameter) and high surface energy, CNTs exhibit a strong tendency to agglomerate into bundles resembling spaghetti-like entanglements. It is practically impossible to achieve an arrangement in which all nano-tubes are oriented transversely to the sliding direction to realise a true rolling-bearing effect. So how does the protective mechanism of CNTs operate? The effect seems to be similar to that observed for graphene flakes. During friction and the relative sliding of the contacting surfaces, CNTs undergo gradual degradation and exfoliation, leading to the formation of two-dimensional structures resembling graphene sheets. These tribologically generated layers then slide over one another as incommensurate surfaces, thereby significantly reducing friction and wear [48-50].

The pronounced tendency of CNTs to agglomerate may also account for their detrimental effects on friction and wear. When poorly dispersed, CNTs can cluster into large carbonaceous agglomerates, which behave as undesired third bodies in the contact. Such agglomerates act as micro-abrasive particles, increasing resistance to motion and promoting surface damage through scratching, ploughing, or fatigue-related mechanisms. Several studies have reported that this effect becomes particularly pronounced at higher CNT concentrations or under insufficient stabilization, highlighting the critical importance of proper dispersion techniques in achieving beneficial tribological outcomes [51-52]. The key issue, therefore, is to formulate lubricants containing CNTs in such a way that their beneficial tribological properties can be exploited while simultaneously preventing excessive agglomeration.

A promising strategy to improve the tribological performance of CNTs is their decoration with metal nanoparticles, whose anti-friction and anti-wear effects are well established. Positive results have been reported for CNT-metal hybrids, specifically with silver [53], copper [50,54], and nickel [54,55], outperforming oils containing only CNTs or only metal nanoparticles, achieving lower friction and wear at equivalent concentrations. Considering both the benefits and drawbacks of CNTs as effective yet difficult-to-control tribological additives, this study proposes the formulation of a new generation of hybrid greases. For this purpose, we developed a composition that combines the excellent anti-friction properties of IL with nickel-decorated CNTs, serving respectively as the liquid phase and the tribo-active thickener. This hybrid system was applied to lubricate polymer-steel friction pairs, and its performance in reducing friction and wear was benchmarked against a commercially available reference grease.

2. Materials and methods

2.1. Fabrication of hybrid greases

For this study, we proposed a proprietary formulation of a hybrid grease, in which the liquid phase was IL and the thickener consisted of multi-walled CNTs (MWCNTs). Commercially available MWCNTs, NC7000™ (Nanocyl Co. Ltd., Sambreville, Belgium), were employed. According to the manufacturer's specifications, the composition of the MWCNTs was approximately 90 wt.% carbon, ~9 wt.% Al_2O_3 support, and ~1 wt.% iron-based catalyst. The dimensional characteristics were also specified: an average length of 1.5 μm and a diameter of 9.5 nm. The presence of Al_2-O_3 originates from the manufacturing process of MWCNTs, where it acts as a support material for the metal catalyst during nanotube growth by chemical vapour deposition (CVD). Such residual alumina is commonly observed in MWCNTs produced by CVD and reflects the role of oxide supports in stabilising and dispersing the active catalyst particles during synthesis. However, the presence of such impurities is undesirable from the standpoint of tribological performance. Al_2O_3 is characterised by high hardness, and even at the nanoscale, it can significantly influence wear mechanisms within the contact through its abrasive action. To mitigate this effect, the MWCNTs were purified to remove Al_2O_3before blending with the liquid phase, as described in [50].

The purified MWCNTs were subsequently functionalized through nickel decoration. Nickel was selected due to its ability to improve the dispersion and thermal stability of the nanotubes, as well as to mitigate agglomeration, thereby offering the potential to enhance their tribological performance [56,57]. The Ni-decorated CNTs (Ni-CNTs) were synthesised following a modified NanoLab, Inc. (Waltham, USA) procedure. Briefly, 1.00 g of CNTs was dispersed in 20 mL of sensitiser solution (0.50 g $SnCl_2$ in 4 mL of 38% $HCl_{(aq)}$ and 96 mL deionised water) using a Sonics VC505 ultrasonic horn. The suspension was centrifuged at 7000 rpm for 5 min (Dupont Sorvall Microspin 24S), washed with deionised water, and the wash/centrifugation cycle repeated three times. The wet CNTs were then re-suspended in 20 mL of activator solution (0.03 g $PdCl_2$ in 0.3 mL of 38% HCl and 99.7 mL deionised water), sonicated, centrifuged, and washed three times. Subsequently, the CNTs were introduced into 100 mL of electroless deposition (ELD) solution (3.00 g $NiSO_4 \cdot 6H_2O$, 2.50 g sodium hypophosphite hydrate, 0.30 g boric acid, 1.00 g sodium acetate, 1.00 g sodium citrate dihydrate in 100 mL deionised water) and maintained at 80-95 °C under sonication (5 min) to prevent clustering. After the reaction, the product was centrifuged and washed repeatedly, filtered, and dried under vacuum at 80 °C overnight. All reagents were of analytical grade and used as received (Alfa Aesar, Acros Organics).

Trihexyltetradecylphosphonium bis(2-ethylhexyl)phosphate (P_{66614} DEHP, $C_{48}H_{102}O_4P_2$) was selected as the liquid phase. This IL is a well-known oil additive with documented anti-friction, anti-wear, and anti-corrosion properties [58,59]. Nevertheless, its use as the liquid phase in lubricating greases has not been reported to date.

To achieve a homogeneous dispersion of MWCNTs in IL, a homogenisation method was applied using a Unidrive X1000 homogeniser equipped with a G20 tip. The samples were subjected to shear forces at 20,000 rpm in three 30-second cycles. Six grease formulations were prepared: three with Ni-decorated CNTs (IL + Ni-CNTs at 0.1, 0.5, and 0.75 wt.%) and three with non-decorated CNTs (IL + CNTs at 0.10, 0.50, and 0.75 wt.%).

2.2. Tribological tests and wear analyses

Tribological experiments were conducted using a block-on-ring tribometer (Figure 1). The rings, machined from AISI 4130 steel, had a ground cylindrical surface finish (Sa ≈ 0.5 μm), an outer diameter of 45 mm, and a width of 12 mm. Polymer blocks (15 × 10 × 6 mm) were prepared from commercially available friction-grade materials: UHMWPE (Tivar 1000) and PA-6 (Ertalon 6SA). The block contact surfaces (15 × 10 mm) were ground to achieve comparable roughness.

Tests were performed under kinetic sliding conditions with the following parameters: ring rotation speed of 200 rpm, normal loads of 250, 500, and 750 N, and a test duration of 30 min. To reduce the risk of rapid polymer damage at the beginning of the experiment, the load was gradually increased in steps of 250 N per minute until the target value was reached (Figure 1). In each case, 0.1 mL of lubricant was applied. The lubricants under study included the hybrid greases formulated in Section 2.1, the pure IL, and, as a benchmark, a commercial polyurea-thickened poly(alpha-olefin)- (PAO-) based grease recommended for polymer contacts.

Frictional response was assessed based on the measured friction torque, from which the coefficient of friction (COF) was calculated at one-minute intervals. For statistical reliability, each material–lubricant configuration was tested three times. After testing, the excessive lubricant was removed from the specimen surfaces using lint-free wipes. No further chemical cleaning was performed before wear evaluation.

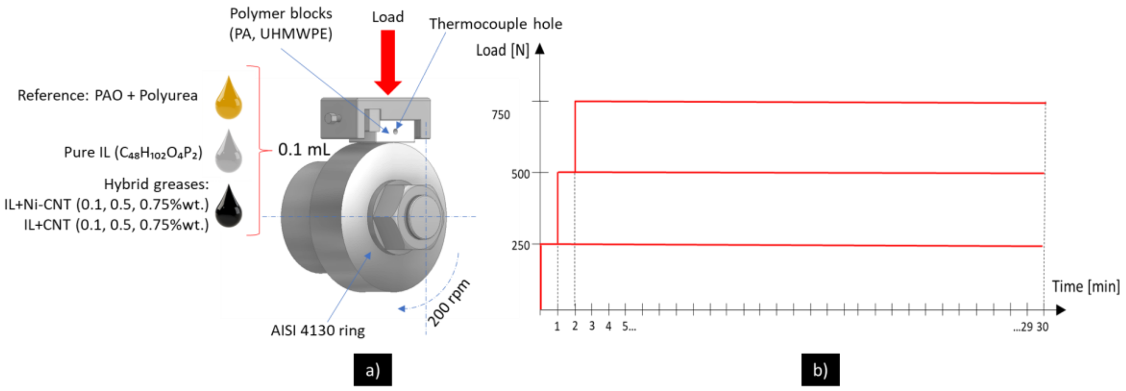

Figure 1. Material configurations and tribological test conditions (a); load application diagram (b).

SEM (FEI Quanta 250 FEG) and EDS (Ametek/Edax Octane Pro) analyses were performed for each polymer type, examining randomly selected working surfaces of unused samples as well as wear tracks on the blocks after tribological testing. The same procedure was applied to the steel rings, focusing on the contact surfaces that had interacted with each polymer. These investigations provided the basis for identifying and characterising the wear mechanisms of both the polymer and steel specimens.

Non-polarised Raman spectra of PA, UHMWPE, CNT, Ni-CNT, and samples after the friction process were measured using a Renishaw inVia Raman microscope. The spectra were recorded using laser light of 785 nm wavelength in the range 100-3200 cm^{-1} with a spectral resolution better than 2 cm^{-1}. The power of the laser beam focused on the sample with a 50× objective was kept below 10 mW. The position of peaks was calibrated before collecting the data using a Si crystalline sample as an internal standard. The bands' positions were determined by using the fitting package of the Wire 3.4 software.

Areal topographic measurements were performed using a 3D contact profilometer (Jenoptik T8000) on both new and worn surfaces of the polymer samples. A needle with a 2 μm tip radius was used for the measurement. The surface topography was evaluated in terms of standardized height and volumetric parameters in accordance with ISO 25178 [60], using MountainsMap® 10 software.

The surface free energy (SFE) of the polymers was determined from contact angle measurements performed with model liquids (water and diiodomethane) on both new and worn surfaces. Wettability was assessed using an Attension Biolin goniometer, and each surface was tested in triplicate. The Owens-Wendt-Rabel-Kaelble (OWRK) method was applied to calculate the total SFE as well as its dispersive and polar components [61].

3. Results and discussion

The Results and Discussion section is organised into six parts, addressing decoration efficiency, friction behaviour, wear analysis by SEM/EDS, wear characterisation by Raman spectroscopy, surface free energy, and surface topography.

3.1. Characterization of Ni-decorated CNTs

Figure 2 presents the transmission electron microscopy (TEM) image and energy-dispersive X-ray (EDX) spectroscopy analysis of CNTs decorated with nickel. The efficiency of the decoration process can be considered moderate, as Ni nanoparticles are not uniformly distributed along the CNT mesh but rather form local “wrap-like” clusters that partially envelop the nanotubes longitudinally. The EDX analysis performed at five points containing nickel-functionalized regions confirmed the presence of Ni, with its weight fraction ranging from 22.32% to 59.73% and atomic fraction from 6.50% to 63.19%. (EDX Cu-signals originate from copper mesh TEM substrates). Such a non-uniform distribution suggests partial surface coverage, which may locally modify the electronic and tribochemical activity of the CNTs and, in turn, influence their behaviour when incorporated into the lubricant matrix.

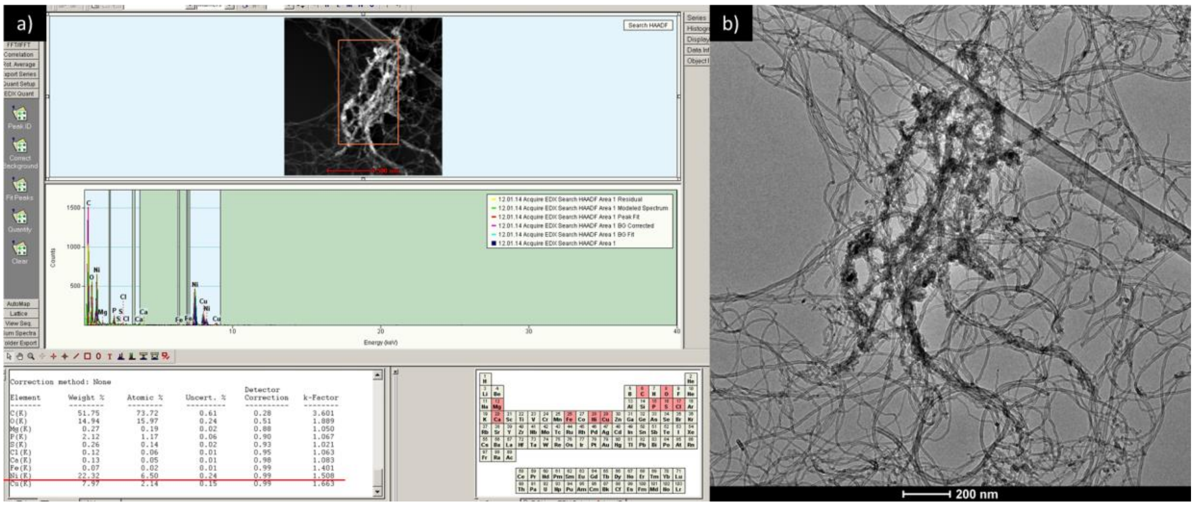

```
Correction method: None

                                           Detector
Element     Weight %    Atomic %    Uncert. %   Correction   k-Factor
-------     --------    --------    ---------   ----------   --------
C(K)          51.75       73.72       0.61         0.28        3.601
O(K)          14.94       15.97       0.24         0.51        1.889
Mg(K)          0.27        0.19       0.02         0.88        1.050
P(K)           2.12        1.17       0.06         0.90        1.067
S(K)           0.26        0.14       0.02         0.93        1.021
Cl(K)          0.12        0.06       0.01         0.95        1.063
Ca(K)          0.13        0.05       0.01         0.98        1.083
Fe(K)          0.07        0.02       0.01         0.99        1.401
Ni(K)         22.32        6.50       0.24         0.99        1.508
Cu(K)          7.97        2.14       0.15         0.99        1.663
```

Figure 2. Selected EDX analysis (a) and TEM image (b) of CNTs decorated with nickel.

3.2. Friction tests

Figures 3-5 present the averaged COF curves for the reference grease, the neat ionic liquid, and the hybrid greases with Ni-decorated and non-decorated CNTs, obtained for the PA-AISI4130 pair under loads of 250, 500, and 750 N. For clarity, statistical deviations are not shown in the graphs. It should be noted that all lubricants formulated with the IL demonstrated a markedly reduced COF. Furthermore, in each of case, the COF exhibited substantially higher stability than the reference grease, particularly during the 10-30 min interval of the test. Considering the final stage of the test (30 min) at the lowest load (250 N, Figure 3a), the highest frictional resistance was recorded for the reference grease (COF = 0.0978), while the lowest was observed for the hybrid containing a medium concentration of Ni-CNTs (0.5 wt.%), with a COF of 0.0237. This corresponds to a friction reduction of approximately 76%. Other IL-based lubricants also led to a substantial decrease in frictional resistance: about 73% for the remaining hybrids (COF = 0.0267) and about 70% for the pure IL (COF = 0.0296). For the tests conducted under higher loads (500 N – Figure 4a, 750 N – Figure 5a), a similar trend was observed. At 500 N, the COF decreased from 0.0741 for the reference grease to 0.0207 for the IL + Ni-CNTs (0.5 wt.%) formulation, corresponding to a friction reduction of approximately 72%. A similar effect was obtained under a load of 750 N, where the COF dropped from 0.0662 to 0.0168, giving a reduction of about 75%. An important observation is that, with increasing load, a decrease in COF values was recorded for most of the lubricants tested. For example, in the case of the reference grease, the COF decreased by about 32%, from 0.0978 at 250 N to 0.0662 at 750 N. For the pure IL, the reduction was approximately 13% (from 0.0296 to 0.0257), while for the most effective hybrid (IL + Ni-CNTs, 0.5 % wt.), the COF decreased by about 29%, from 0.0237 to 0.0168. This behaviour is related to the protective mechanisms inherent to each lubricant, which will be discussed in detail in the subsequent sections.

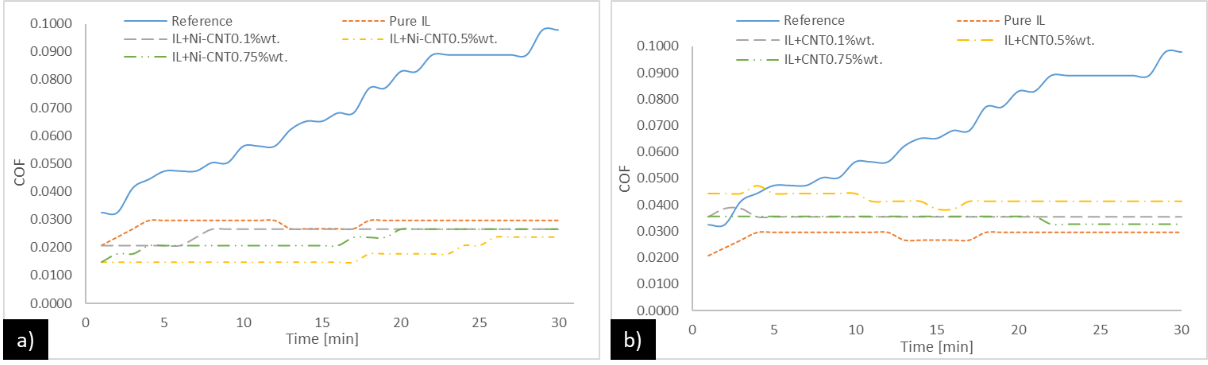

Figure 3. Averaged COF trends for the AISI 4130-PA friction pair under a load of 250 N: (a) hybrid greases with Ni-decorated CNTs; (b) hybrid greases with non-decorated CNTs.

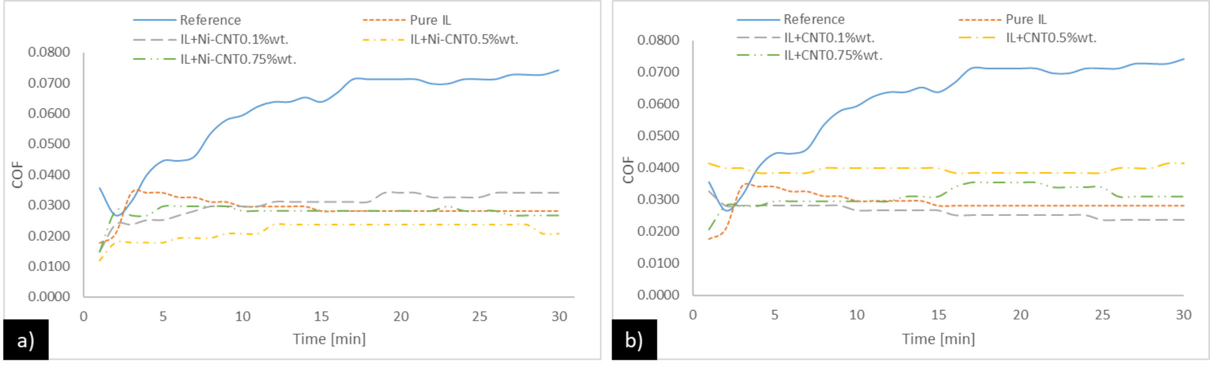

Figure 4. Averaged COF trends for the AISI 4130-PA friction pair under a load of 500 N: (a) hybrid greases with Ni-decorated CNTs; (b) hybrid greases with non-decorated CNTs.

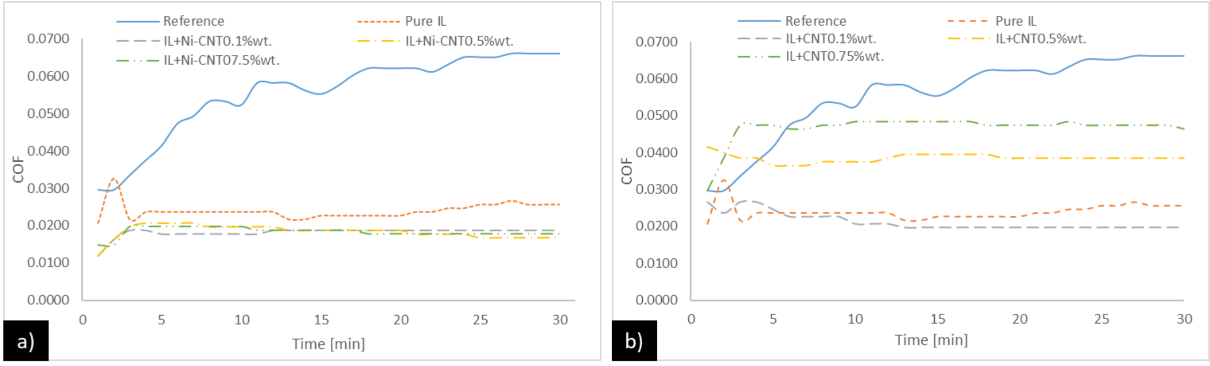

Figure 5. Averaged COF trends for the AISI 4130-PA friction pair under a load of 750 N: (a) hybrid greases with Ni-decorated CNTs; (b) hybrid greases with non-decorated CNTs.

The situation is somewhat different for the hybrid greases thickened with non-decorated CNTs. Although all of these lubricants (including the neat IL) significantly reduced the COF compared to the reference, the addition of CNTs alone did not provide any further improvement over the neat IL and in most cases resulted in slightly higher COF values. Only under higher loads (500 and 750 N) was a beneficial effect observed for the lowest CNT concentration in IL (0.1 wt.%). In contrast, at these loads, higher concentrations of pristine CNTs led to a deterioration of the frictional conditions.

To highlight the stable frictional behaviour observed between 10 and 30 min, the mean COF values calculated over this interval are plotted (Figure 6) as a function of load for all IL-based lubricants, with standard error bars included. This representation enables a clearer comparison of their performance under different loading conditions, while minimising the influence of initial transients. Since only three load levels were tested, no mathematical fitting was applied – the connecting line serves as a graphical aid only.

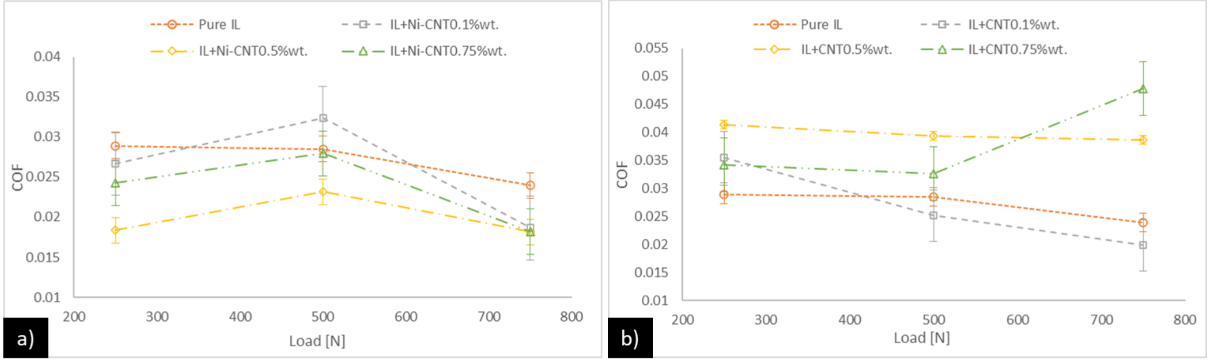

Figure 6. Averaged COF trends for the AISI 4130-PA friction pair as a function of load: (a) hybrid greases with Ni-decorated CNTs; (b) hybrid greases with non-decorated CNTs.

A general decrease in COF with increasing load is observed for all lubricants, except for the hybrid containing 0.1 wt. % Ni-CNTs, which shows a local maximum at 500 N. The hybrid with 0.5 wt. % Ni-CNTs consistently demonstrates the lowest COF across the entire load range, which may result from a favourable balance between the formation of boundary films and the potential abrasive effect of nanoparticles. At the highest load (750 N), all hybrid lubricants achieve markedly lower friction than the pure ionic liquid, confirming the beneficial tribological contribution of Ni-decorated CNTs under high contact pressure.

Figures 7-9 present the averaged COF trends for the reference grease, the neat IL, and the hybrid greases with Ni-decorated and non-decorated CNTs, obtained for the UHMWPE-AISI4130 pair under loads of 250, 500, and 750 N. For clarity, statistical deviations are not shown in the graphs.

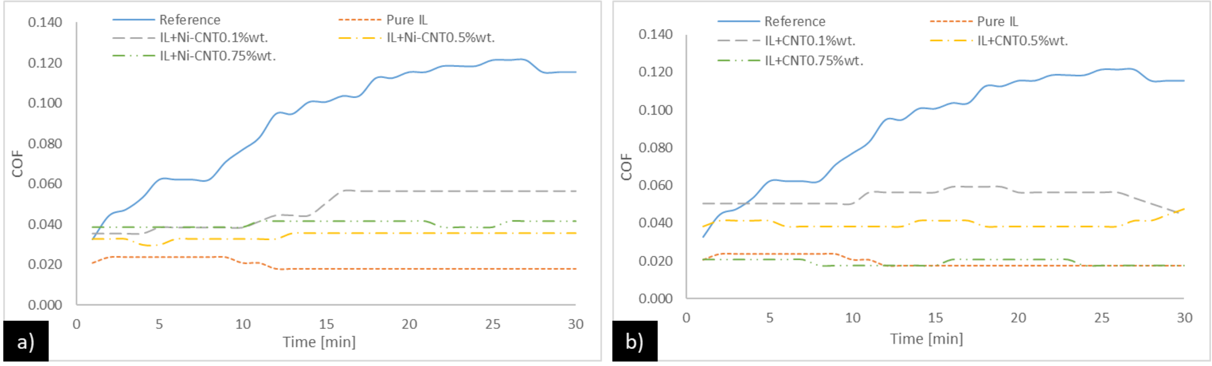

Figure 7. Averaged COF trends for the AISI 4130-UHMWPE friction pair under a load of 250 N: (a) hybrid greases with Ni-decorated CNTs; (b) hybrid greases with non-decorated CNTs.

It should first be noted that, similarly to the steel–polyamide friction pair, a significant reduction in the COF is also observed here for all lubricants based on the IL, compared with the reference grease. In addition, their frictional behaviour is much more stable than that of the reference, and in most cases the COF stabilises, between 10 and 15 minutes of testing. The exceptions are hybrid lubricants with higher CNT contents, namely IL + Ni-CNTs 0.75 wt.% and IL+CNTs 0.5 and 0.75 wt.%, which, under the highest load (750 N), exhibit a gradual increase in friction and less stable performance – although still markedly better than the reference. A notable difference, however, can be observed between the frictional behaviour of the IL-based hybrids containing Ni-CNTs or CNTs and that of the neat IL. For this material configuration (AISI4130-UHMWPE), optimal lubrication was achieved with the neat IL under all load conditions: 250 N → COF = 0.0178, 500 N → COF = 0.0193, and 750 N → COF = 0.0207. At a load of 250 N, all IL-based lubricants significantly reduced the COF compared with the reference grease, with reductions ranging from approximately 50% to 85%. The neat IL and the hybrid containing 0.75 wt.% of pristine CNTs provided the lowest COF (0.0178), representing an 85% reduction relative to the reference. In contrast, other CNTs- and Ni-CNTs-enriched hybrids exhibited higher friction than the neat IL, indicating that at low load, the presence of nano-additives does not improve, and may even hinder, the formation of stable boundary layers.

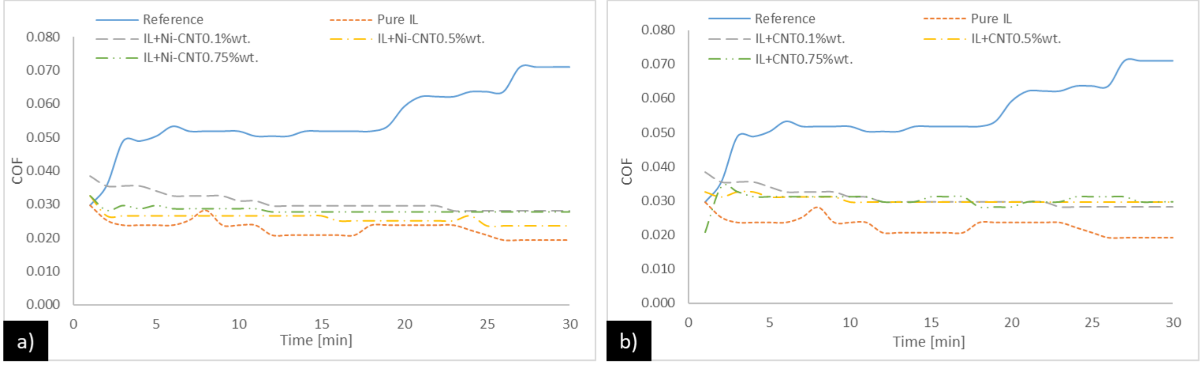

Figure 8. Averaged COF trends for the AISI 4130-UHMWPE friction pair under a load of 500 N: (a) hybrid greases with Ni-decorated CNTs; (b) hybrid greases with non-decorated CNTs.

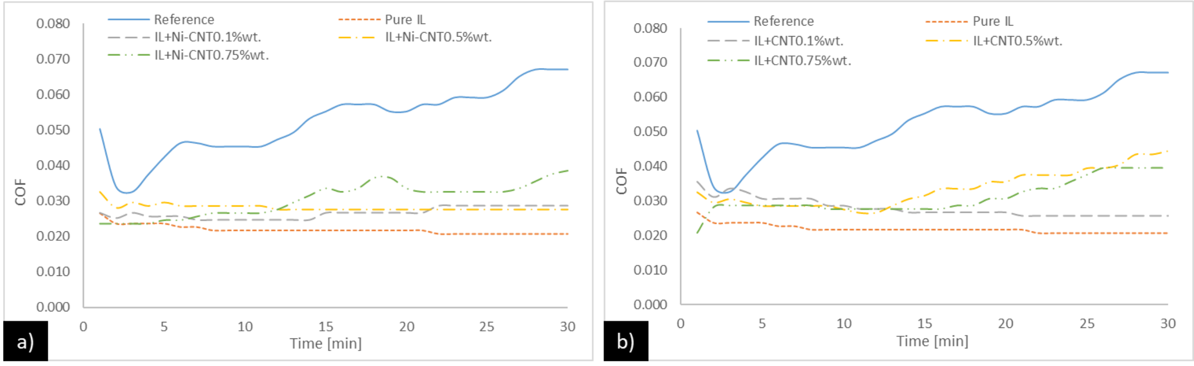

Figure 9. Averaged COF trends for the AISI 4130-UHMWPE friction pair under a load of 750 N: (a) hybrid greases with Ni-decorated CNTs; (b) hybrid greases with non-decorated CNTs.

At 500 N, all IL-based lubricants again provided a considerable reduction in friction compared with the reference, with COF decreases ranging from 58% to 73%. The neat IL maintained the lowest COF (0.0193), confirming its superior lubricating performance in this load range. The addition of CNTs or Ni-CNTs slightly increased the COF, with the smallest deviation observed for IL + Ni-CNT 0.5 % wt., where the COF was only about 23% higher than that of the neat IL. These results suggest that, also at medium loads, the presence of nano-additives does not enhance the antifriction effect of the IL.

At the highest load of 750 N, all IL-based lubricants continued to provide lower friction than the reference, with COF reductions between roughly 35 % and 69 %. The neat IL again exhibited the lowest COF (0.0207), confirming its robust lubricating capability under high contact pressure. Among the hybrids, IL + Ni-CNT 0.5 % wt. and IL + CNT 0.1 % wt. showed the most favourable results, with friction values only 30-40 % higher than the neat IL. In contrast, formulations with higher CNT contents (0.5-0.75 % wt.) revealed a noticeable increase in COF and less stable sliding behaviour, suggesting that excessive nano-additive loading may intensify wear mechanisms within the contact.

Across all loads, the neat IL provided the most effective lubrication for the AISI4130-UHMWPE pair, achieving a 69-85% reduction in COF relative to the reference grease. The addition of CNTs or Ni-CNTs did not further decrease friction. At medium and high loads, the presence of nano-additives slightly increased COF, likely due to weaker adsorption of the boundary layer and mild adhesive–abrasive effects. Only at 250 N did the IL + CNT 0.75 wt. % formulation exhibit a COF identical to that of the neat IL, representing a singular anomaly that may be associated with reduced asperity contact or a transient third-body effect at low load.

Figure 10 presents the average COF values (10-30 min of testing) as a function of load for the AISI 4130-UHMWPE pair lubricated with IL-based formulations containing Ni-CNTs (Fig. 9a) and pristine CNTs (Fig. 9b).

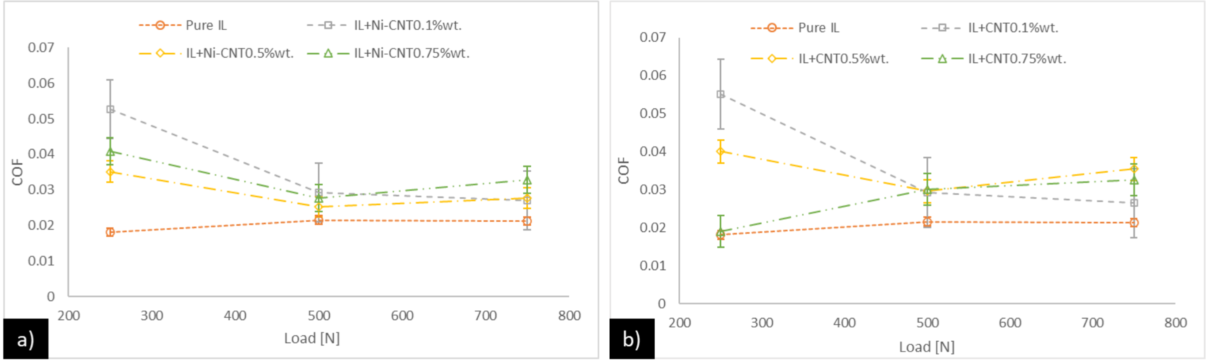

Figure 10. Averaged COF trends for the AISI 4130-UHMWPE friction pair as a function of load: (a) hybrid greases with Ni-decorated CNTs; (b) hybrid greases with non-decorated CNTs.

In both cases, the neat IL exhibited the lowest and most stable friction across the entire load range. For the hybrids, a moderate decrease in COF was observed from 250 to 500 N, followed by slight stabilisation or an increase at 750 N, depending on CNT concentration. The addition of Ni-CNTs resulted in smoother COF trends and slightly improved stability compared to non-decorated CNTs, suggesting enhanced dispersion and boundary film formation. Overall, the results indicate that the frictional behaviour of IL-based hybrids depends primarily on the load-additive balance, with excessive CNT content at higher loads tending to slightly increase COF. However, these differences are not statistically significant.

3.2. Wear mechanisms

This section analyses the wear tracks formed on the polymer blocks and the corresponding steel rings. Various characterization techniques were employed for this purpose, including SEM, EDS, and Raman spectroscopy.

3.2.1 Wear tracks – SEM/EDS analysis

Figure 11 shows SEM images (200×, 500×, and 2000×) of the wear track on the selected PA block (Fig. 11a-c) and the corresponding worn surface of the AISI 4130 ring (Fig. 11d-f). These images correspond to the samples tested at a load of 500 N and lubricated with IL + Ni-CNTs 0.5 % wt.

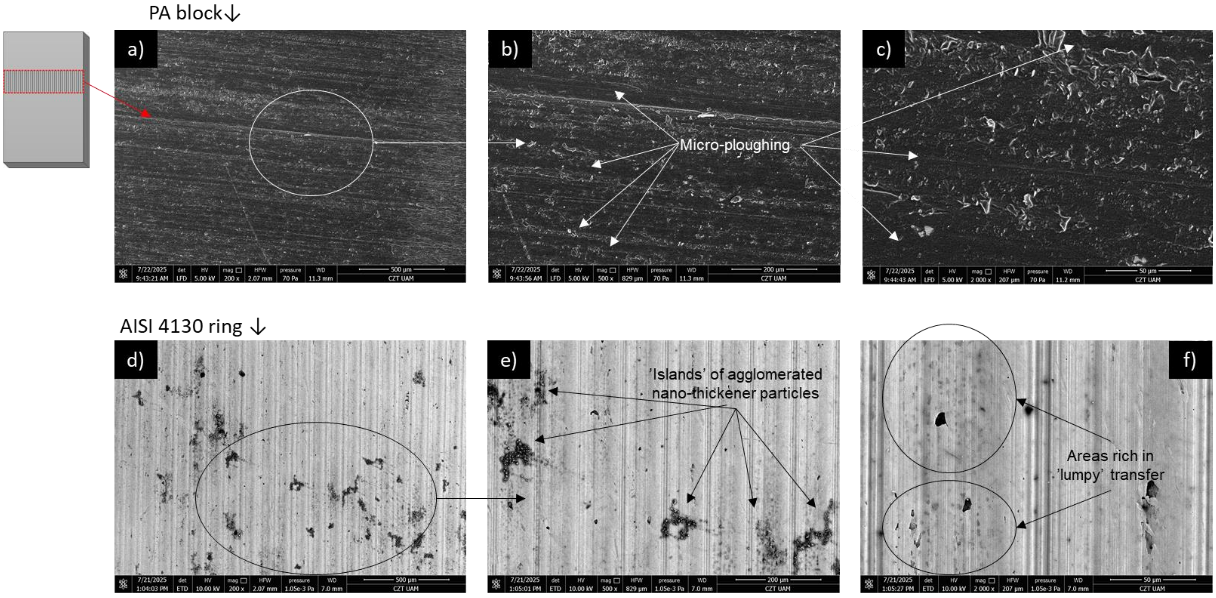

Figure 11. Investigations of wear tracks of PA blocks and AISI4130 rings lubricated with IL + Ni-CNTs 0.5 % wt.: SEM images at different magnifications – 200× (a), 500× (b), and 2000× (c) – and the corresponding AISI 4130 rings: 200× (d), 500× (e), and 2000× (f).

In the case of the PA blocks, the wear traces clearly indicate an abrasive wear mechanism. Distinct grooves can be identified, formed as a result of micro-ploughing, where asperities of the steel counterface plastically deform the polymer surface. On the steel surfaces, small islands of carbon agglomerates can be easily identified. They most likely were formed due to the partial decomposition of the hybrid lubricants and may serve as an additional source of abrasive action on the polymer surface. In addition, the steel surfaces exhibit so-called lumpy transfer, that is, the adhesive deposition of irregular polymer patches onto the steel surface as a result of friction (the characteristic grey "freckles" are most evident in Figure 11f). In principle, this phenomenon is beneficial, as it locally replaces the steel-polymer interface with a polymer-polymer one, for which the frictional conditions are milder. However, for most polymers, including PA, the lumpy transfer results in non-uniform and discontinuous films that do not ensure consistent frictional conditions across the entire contact area [62].

The EDS mapping of the steel rings confirms the formation of lumpy polymer transfer (Figure 12c). Carbon is distributed along the sliding direction and accumulates on the asperity peaks of the steel surface, which are responsible for polymer abrasion, with additional irregular local concentrations detected within the contact. Figures 12b (PA block) and 12e (AISI 4130 ring) show the distribution of phosphorus on the wear tracks. In both cases, the P content is similar, at the level of approximately 4-5 % wt., and the distribution appears mainly aligned with the sliding direction, with additional isolated island-like accumulations. This suggests the formation of phosphorus-containing tribofilms on both contacting surfaces, indicating that the ionic liquid actively participates in tribochemical reactions rather than acting solely as a passive physical separator (hydrodynamic effect). In contrast, the EDS mapping of nickel showed no detectable Ni signal on the PA surface and only a very low average content (~2 % wt.) with a uniform spatial distribution on the steel ring. As this value is close to the detection limit of the method and no localised accumulations were observed, the signal should be interpreted with caution, as it may represent background noise rather than evidence of a true material transfer.

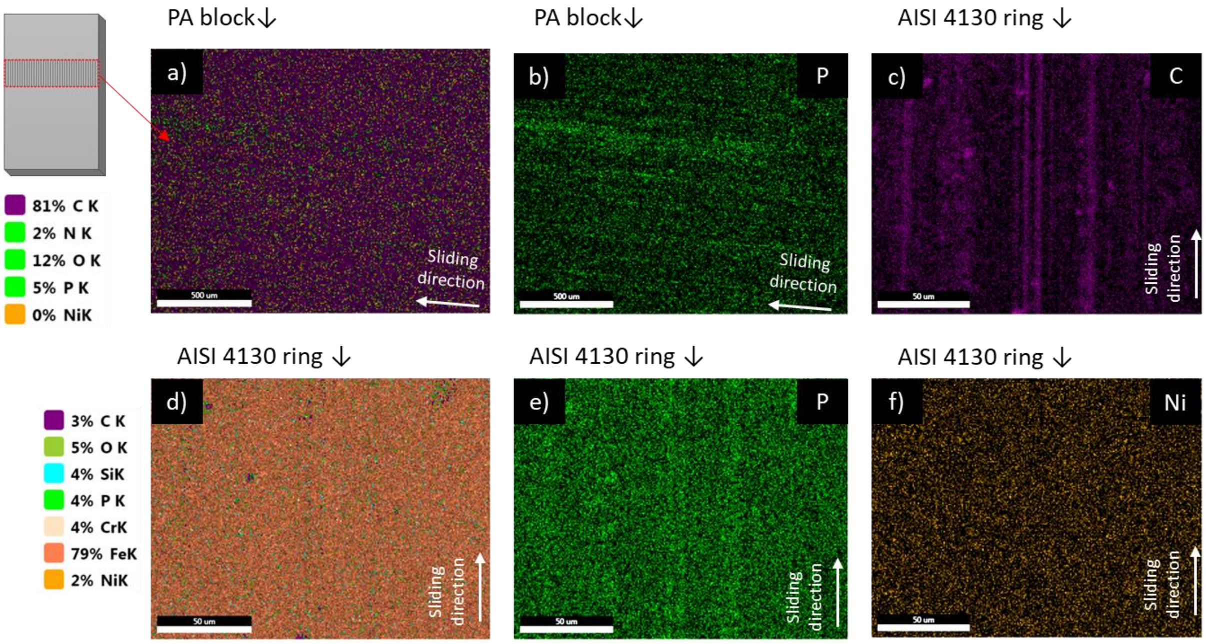

Figure 12. EDS mapping of wear tracks of PA blocks and AISI4130 rings lubricated with IL + Ni-CNTs 0.5 % wt.: a) PA block – general view; b) PA block – phosphorus distribution; c) AISI4130 ring – carbon distribution; d) AISI4130 ring – general view; e) AISI4130 – phosphorus distribution; f) AISI4130 ring – nickel distribution.

Figure 13 shows SEM images (200×, 500×, and 2000×) of the wear track on the selected UHMWPE block (Fig. 13a-c) and the corresponding worn surface of the AISI 4130 ring (Fig. 13d-f). These images correspond to the samples tested at a load of 500 N and lubricated with IL + Ni-CNTs 0.5 % wt. In the case of UHMWPE, the wear mechanism differs from that observed for PA. Instead of a clear abrasive pattern, longitudinal and irregular material losses are visible, which appear to be of an adhesive nature. This indicates a more dynamic lumpy transfer process and more intensive polymer deposition onto the steel surface. This observation is supported both by the SEM images (Figure 13f), which show more pronounced polymer transfer streaks, and by the EDS mapping (Figure 14c), which confirms the localised nature of the 'lumpy' transfer and its higher content (by ~9 wt.%) compared with the AISI 4130 ring surfaces lubricated with the hybrid lubricants in contact with PA. The adhesive nature of wear is also evidenced by the presence of post-adhesive polymer stubs, torn off during plastic deformation as the material was transferred onto the ring surface. Such features are characteristic of adhesive wear dominated by localised material pull-out rather than uniform abrasive removal.

Figure 14 shows the EDS mapping of the wear tracks on the UHMWPE surface and the corresponding AISI 4130 steel ring. Alongside the above described carbon distribution, the P and Ni maps closely resemble those obtained for the PA-AISI 4130 pair. The phosphorus content is at a comparable level (~5 wt.% on the steel surface and around ~6 wt.% on the polymer), and its distribution aligns mainly along the asperity peaks of the AISI 4130 surface. In contrast, the Ni signal on the steel surface was detected at around 2 wt.%, but its uniform spatial distribution, lack of directional features and absence of localised accumulations indicate that it should be regarded as background noise rather than evidence of actual Ni transfer. No nickel was detected on the UHMWPE surface. This suggests that the tribochemical activity within the contact zone is primarily governed by the phosphorus-containing anion of the ionic liquid, while the Ni introduced as the CNTs decoration does not actively contribute to boundary film formation.

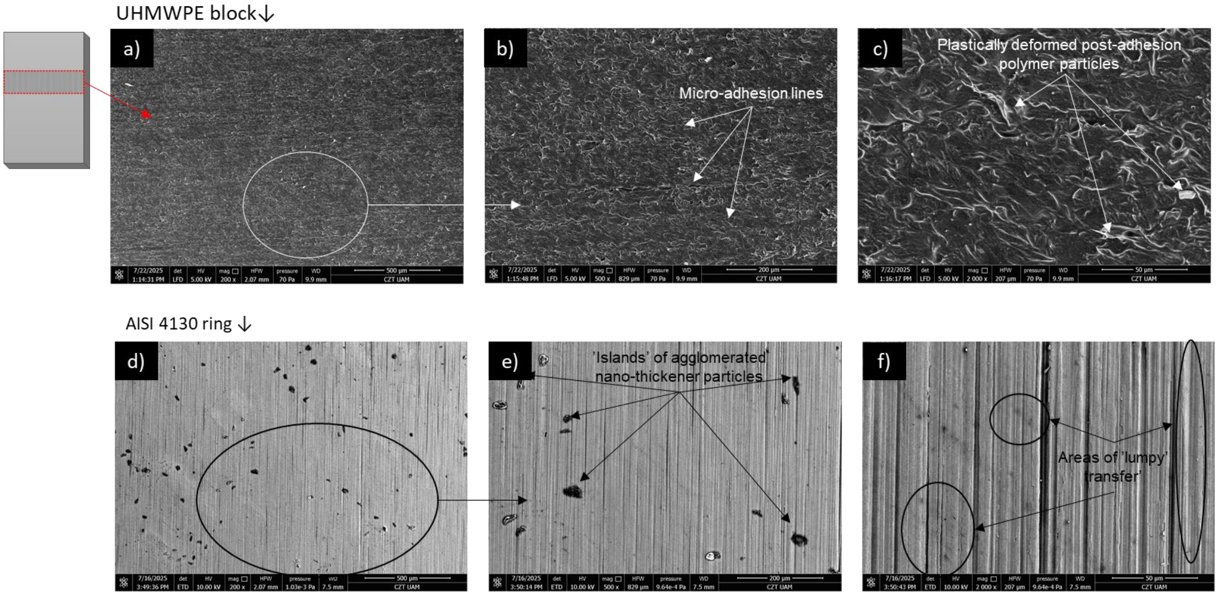

Figure 13. Investigations of wear tracks of UHMWPE blocks and AISI4130 rings lubricated with IL + Ni-CNTs 0.5 % wt.: SEM images at different magnifications – 200× (a), 500× (b), and 2000× (c) – and the corresponding AISI 4130 rings: 200× (d), 500× (e), and 2000× (f).

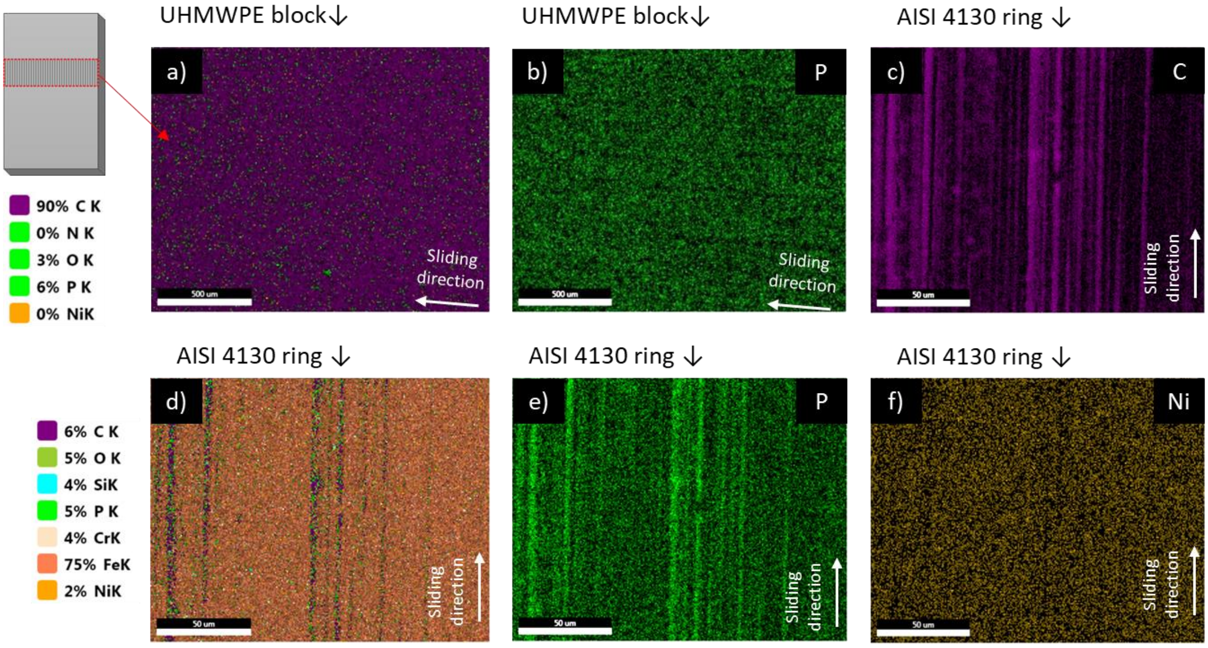

Figure 14. EDS mapping of wear tracks of UHMWPE blocks and AISI4130 rings lubricated with IL + Ni-CNTs 0.5 % wt.: a) PA block – general view; b) PA block – phosphorus distribution; c) AISI4130 ring – carbon distribution; d) AISI4130 ring – general view; e) AISI4130 – phosphorus distribution; f) AISI4130 ring – nickel distribution.

Despite the similar appearance of the wear track composition on the EDS maps for both the steel surfaces and their corresponding polymer counterparts, the frictional behaviour in the two material configurations is markedly different. This raises fundamental questions: what is the origin of this discrepancy, and what is the actual role of CNTs and their Ni decoration during sliding? To address this, high-magnification SEM observations of the steel surfaces (100,000×) were performed, as presented in Figure 15.

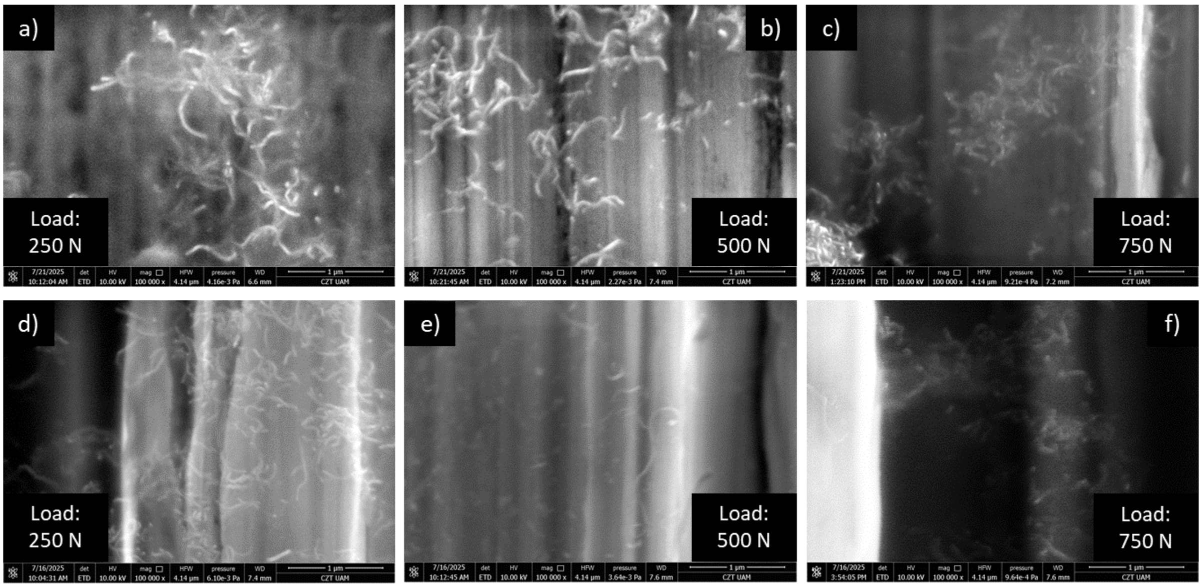

Figure 15. High-magnification SEM images (100,000×) of Ni-decorated CNT residue on the AISI 4130 ring surfaces in contact with: (a) PA, 250 N; (b) PA, 500 N; (c) PA, 750 N; (d) UHMWPE, 250 N; (e) UHMWPE, 500 N; (f) UHMWPE, 750 N.

In the PA-AISI 4130 configuration (Figure 15a-c), a pronounced deformation of the Ni-decorated CNT network is observed. Characteristic bright spots can be identified with two distinct morphologies: isolated point-like signals, indicating mechanically fractured CNTs, and elongated signals along individual nanotubes, which suggest damage to the nickel wrapping or partial exfoliation of the CNT walls. This is a crucial observation from the friction reduction perspective. Mechanical damage and exfoliation of the CNTs generate carbonaceous flakes resembling graphene-like sheets, whose mutual sliding is associated with extremely low shear resistance, thereby contributing to the decrease in COF at higher loads. In this process, Ni plays a triple role. First, mechanically damaged CNTs exhibit enhanced surface activity and tend to form carbon agglomerates, while the presence of Ni acts as a physical spacer that hinders such aggregation and instead promotes weak sliding interactions between exfoliated carbon flakes. Second, Ni may facilitate more efficient heat dissipation from the contact, further stabilising the tribo-layer. This effect is corroborated by the measured temperature recorded within the PA block, at mid-thickness (Figure 2), during steady-state sliding (10-30 min interval). At 250 N, the average contact temperature decreased from 39.4 °C for the reference grease to 30.0-30.9 °C for the IL-based formulations, reaching the lowest value (29.3 °C) for IL + 0.75 % wt. of Ni-CNTs. With increasing load, the temperature difference became even more pronounced: at 500 N, it dropped from 45.4 °C (reference) to ~33 °C for the hybrids, and at 750 N from 54.9 °C to only ~32 °C. This consistent reduction in operating temperature indicates that Ni-decorated CNTs not only enhance the thermal conductivity of the tribolayer but also promote more stable shear conditions, limiting local flash temperature rise and thereby improving the overall thermal balance of the contact. Eventually, Ni nanoparticles play a catalytical role as, in the presence of air, they catalyse a gradual oxidative degradation of CNT walls progressing from the edge- and defect-located ‘hot spots’ leading to CNT unzipping and gaseous products as CO and CO_2. This behaviour is extensively supported by ILs of high CNT-individualising potential [63-65].

In contrast, in the case of pristine CNTs, the absence of the Ni “isolating shell” allows more extensive agglomeration of carbon debris, leading to larger abrasive clusters that interact more aggressively with the polymer surface. As a result, the COF remains higher compared to systems containing Ni-decorated CNTs.

In the UHMWPE-AISI 4130 configuration (Figure 15d-f), a different post-friction morphology of CNTs is observed. The CNT mesh appears more relaxed and loosely arranged, but the nanotubes themselves are not as severely deformed as in the PA-steel pair. This is likely related to the different wear mechanism of UHMWPE. Due to the more intensive lumpy transfer, CNTs do not enter the contact directly but instead become partially embedded in the plastically flowing polymer, which hinders their exfoliation and the formation of graphene-like lamellae. Moreover, no clear distinction can be made between the IL + CNT and IL + Ni-CNT lubrication cases in this configuration. The final COF values differ slightly but exhibit a rather random pattern, which is likely a consequence of the stochastic nature of CNT release from the transfer film and their occasional entry into the direct contact zone, where deformation can occur. As a consequence, the neat IL provides the most stable anti-friction behaviour in the UHMWPE system.

3.2.2 Raman spectroscopy

Give that EDS alone may not be sufficient to conclusively detect trace amounts of Ni or to differentiate between carbonaceous wear debris and polymer-derived residues, Raman spectroscopy was employed as a complementary technique. It served two purposes: firstly, to verify the presence or absence of nickel-related signatures on the polymer wear tracks, and secondly, to characterise the nature and structural order of the carbon-based nanostructures present in the same regions.

However, as a preliminary step, Raman spectroscopy was applied to the raw CNT powder and its Ni-decorated counterpart to confirm the structural condition of the additives before their incorporation into the lubricant formulations. In carbon allotropes containing both sp^2 and sp^3 C–C bonding, two characteristic Raman bands are typically observed: the G band at around 1580 cm^{-1}, attributed to the in-plane stretching of sp^2-hybridised carbon atoms, and the D band near 1350 cm^{-1}, which is activated by lattice disorder. At higher wavenumber, a second-order 2D (also referred to as G′) band appears around 2650 cm^{-1}. Moreover, the D band originates from a defect-activated double-resonance scattering process involving phonons from the graphite dispersion curve, which explains its excitation-dependent behaviour and sensitivity to structural imperfections [66-67]. The Raman spectra of CNTs and Ni-CNTs recorded upon excitation with a 785 nm laser are presented in Figure 16. The positions of the D, G and 2D bands were identified at 1305, 1605 and ~2600 cm^{-1} respectively, which is consistent with the expected dispersion-related down-shift under near-infrared excitation.

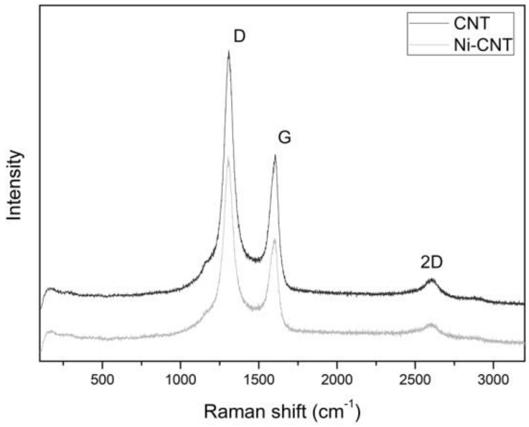

Figure 16. Raman spectra of CNTs and Ni-CNTs recorded upon excitation with 785 nm wavelength.

Raman spectroscopy also enables the evaluation of structural disorder by calculating the intensity ratio I_D/I_G. The I_D/I_G ratio was 1.742 for the pristine CNT powder and 1.852 for the Ni-CNTs, corresponding to an approximate 6% increase in defect density after nickel decoration [68]. This moderate increase in structural disorder suggests the generation of additional edge sites or disrupted graphitic domains, which may later facilitate exfoliation and flake formation under tribological loading.

Figure 17 presents the Raman spectra of the polymer surfaces after the friction tests, shown separately for the PA-based system (17a) and the UHMWPE-based system (17b).

For PA, the Raman spectrum of the pure polymer (Figure 16a, spectrum 1) displays the expected fingerprint features and a broad multicomponent envelope at 2800-3000 cm^{-1}. The bands at 1058, 1079 and 1122 cm^{-1} are assigned to C–C stretching of the α-, β- and γ-phase, while Amide III appears at ~1277 cm^{-1} while the bands at ~1302, ~1370 and ~1440 cm^{-1} correspond to CH$_2$ twisting, wagging and bending, and those at ~1468 and ~1636 cm^{-1} to CNH bending and Amide I, respectively [69]. After sliding at 750 N, the spectra of the wear tracks lubricated with IL + CNTs (Figure 17a, spectrum 2) and IL + Ni-CNTs (Figure 17a, spectrum 3) show an overall intensity increase attributable to the carbonaceous phase and a subtle broadening of Amide I, consistent with tribo-induced disruption of hydrogen-bonded amide domains and conformational disorder of PA chains. Because the polymer bands in the 1300-1650 cm^{-1} region overlap with the CNT D/G features, reliable deconvolution of CNT-related peaks, and hence I_D/I_G, was not attempted. Accordingly, the structural assessment of CNTs relies on powder Raman, whereas their role in the contact is interpreted from SEM/EDS investigations.

The Raman spectra of pure UHMWPE (spectrum 1) and of the wear-track samples lubricated with IL + CNT (spectrum 2) and IL + Ni-CNT (spectrum 3) are shown in Figure 17b. The spectrum of the pure polymer is dominated by two active ranges: 1000-1500 cm^{-1} and 2800–2950 cm^{-1}. The symmetric and antisymmetric CH_2 stretching modes appear at 2882 cm^{-1} and 2845 cm^{-1}, respectively, while the fingerprint region begins with a sequence of CH_2 deformation bands between 1460 and 1060 cm^{-1}. The symmetric deformation vibration modes are located at 1438 cm^{-1} and 1415 cm^{-1}, along with wagging, twisting and rocking modes at 1368, 1295 and 1168 cm^{-1}, respectively. The C–C stretching features at 1127, 1079 and 1062 cm^{-1} are also clearly observed [70-71].

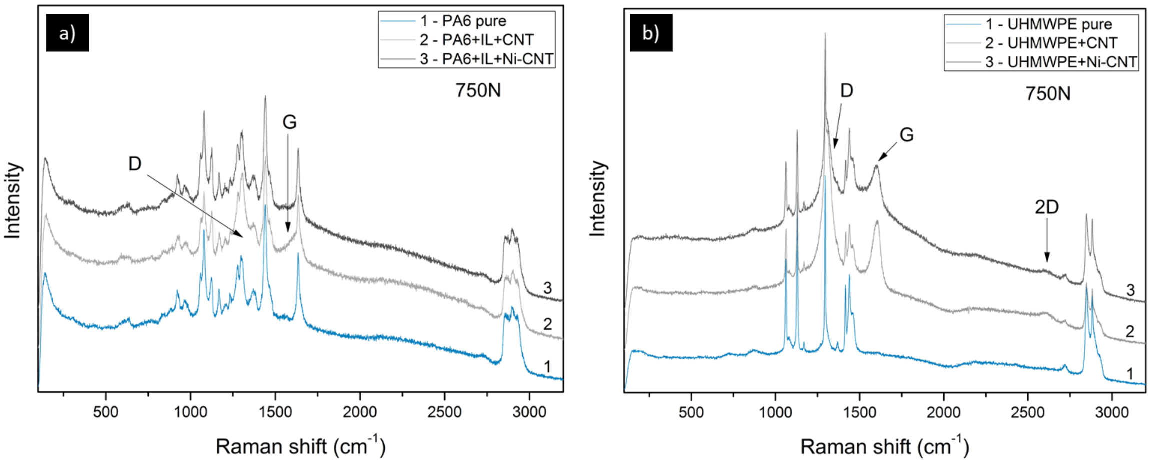

Figure 17. Raman spectra recorded at 785 nm for: a) PA-based samples: 1 - pure PA, 2 - PA lubricated with IL + CNTs, 3 - PA lubricated with IL + Ni-CNTs; (b) 1 - pure UHMWPE, 2 - UHMWPE lubricated with IL + CNTs, 3 - UHMWPE lubricated with IL + Ni-CNTs – all recorded after test at 750 N.

In this case, the D band of CNT overlaps with the intense and narrow CH_2 twisting mode, whereas the G band remains distinguishable, giving a measurable carbon-related signal. A very weak 2D band is also detectable near ~2600 cm^{-1}. The I_D/I_G ratios calculated for spectra 2 and 3 are 2.212 and 2.787, respectively.

Raman spectroscopy of the NCs powders confirmed that Ni decoration increases the defect density of CNTs, providing more active edge sites that can facilitate mechanical exfoliation under load. However, the spectra recorded on the worn polymer surfaces reveal that IL, CNTs and Ni-CNTs do not play the same tribochemical role in both systems.

In the PA-IL-CNTs/Ni-CNTs system, the CNT-related Raman bands are obscured by the PA signature, but the increase in carbon background and the structural response of the polymer, when correlated with SEM/EDS evidence, indicate that CNTs become tribo-activated only when IL is present as a carrier phase, allowing partial exfoliation into low-shear carbon lamellae. In this configuration, IL contributes phosphorus-containing tribofilms, while Ni-decorated CNTs provide shear-adaptable nanocarbon debris, and both effects act synergistically to reduce friction.

In contrast, in the UHMWPE–IL–CNT/Ni-CNT system, Raman detects carbon only as a buried, optically distorted phase, with high apparent I_D/I_G ratios resulting from CNTs trapped within the IL-assisted transfer film rather than exfoliated at the interface. Here, IL still forms phosphate-rich tribolayers, but CNTs remain encapsulated and agglomerated, making Ni decoration tribologically ineffective. As a result, IL alone governs friction performance, and the solid phase does not transition into an active lamellar lubricant as it does in the PA system.

Thus, Raman confirms that the beneficial effect of Ni-CNTs is not intrinsic to the additive but emerges only when the contact conditions allow IL-mediated exposure and exfoliation of the carbon phase.

3.2.3 Surface free energy

SFE analyses were performed for the pristine polymer surfaces and for all wear tracks lubricated with IL + Ni-CNT formulations. In addition, one representative IL+ CNT sample (0.5 wt.%) was included to assess whether nickel decoration influences the interfacial behaviour of the carbon phase. This comparative strategy enabled a clear distinction between the tribochemical contribution of IL and the potential tribophysical activation of CNTs induced by nickel decoration.

SFE studies (Figure 18) were carried out to evaluate how the different lubricant formulations modify the interfacial character of PA and UHMWPE after sliding. The fresh PA surface exhibits a total surface energy of approximately 42 mN/m, dominated by the dispersive component (~35 mN/m) and only ~7 mN/m of polar contribution. UHMWPE is even more apolar, with a similar dispersive component but virtually zero polar fraction.

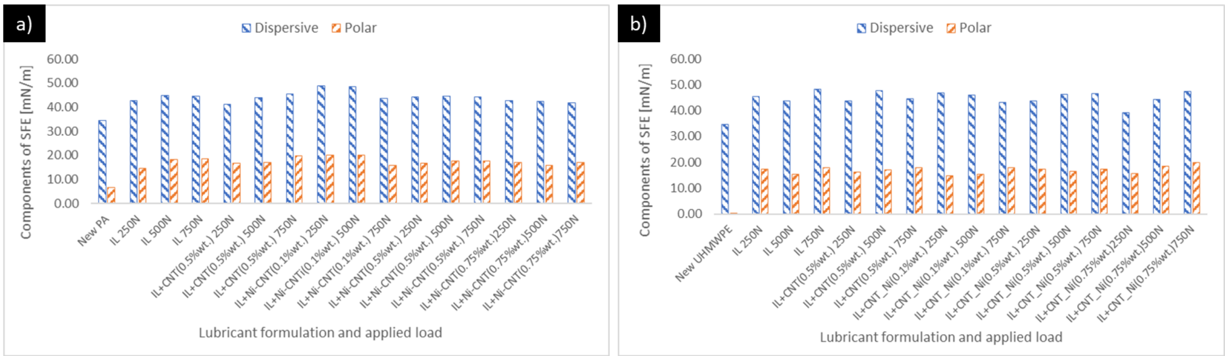

Figure 18. Surface free energy components for the virgin polymer surfaces and wear tracks after tests under different lubrication and load conditions: PA (a), UHMWPE (b).

Upon lubrication with IL and subsequent friction loading, both polymers show a marked increase in the polar component of SFE, reaching values of approximately 15-20 mN/m, while the dispersive component increases to about 43-46 mN/m. This confirms that the IL actively forms a surface tribofilm with polar character, most likely associated with phosphorus-containing reaction products detected in the EDS analysis. A clear divergence in behaviour appears after the addition of CNTs and Ni-CNTs:

- PA: IL + CNTs and IL + Ni-CNTs increase the dispersive component further, but at higher load, especially for IL + Ni-CNTs, a slight decrease in the polar contribution is observed. This shift towards a more apolar surface signature suggests partial coverage of the interface by carbonaceous lamellae formed via CNT fragmentation and exfoliation. In other words, the IL initially activates the surface chemically, but Ni-CNTs subsequently impose a physical shift towards a graphene-like, low-polarity tribolayer, which correlates with the observed drop in COF at high load;
- UHMWPE: Although IL also increases the polar component, the addition of CNTs or Ni-CNTs does not reduce the polar contribution. The surface remains chemically dominated by the IL-derived layer, indicating that CNTs do not emerge as an interfacial phase. This aligns with SEM observations, where CNTs remain embedded within the transfer film, and with Raman results, which show CNT-related bands but without evidence of tribological activation into lamellar structures. Consequently, CNTs do not reduce the surface polarity and do not induce the transition to a low-shear carbon film, explaining why the neat IL remains the most effective lubricant in UHMWPE.

3.2.4 Wear topography

To visualise how the interfacial mechanisms inferred from friction, SFE, and Raman spectroscopy translate into actual surface geometry modification, 3D topography was examined for a reduced but mechanistically representative subset of samples tested at 750 N. For each polymer (PA and UHMWPE), four lubrication conditions were selected: the reference grease (baseline abrasive wear), the neat IL (pure tribochemical film), IL + CNTs 0.75 % wt. (solid phase without Ni activation), and IL + 0.75% Ni-CNTs (Ni-decorated CNT activation).

This selection covers the two limiting cases of interfacial reactivity – from the chemically driven tribofilm formation by the ionic liquid alone to the synergistic Ni-CNT-assisted mechanism – and provides comparison with both the inactive carbon phase (CNT without Ni) and the reference case with a weak tribochemical protection.

It should be noted that 3D surface mapping was carried out once per selected condition. Unlike the friction data, which required statistical averaging, the topographical analysis was used primarily as a morphological indicator, aimed at visualising the dominant wear pattern and quantifying the associated volumetric parameters, rather than to provide averaged roughness statistics.

Figures 19-22 present the 3D surface maps of PA after the 750 N test, together with Abbott–Firestone curves and volumetric parameters (Vmp, Vmc, Vvc, Vvv).

For the reference grease, the worn surface exhibits a strongly valley-dominated topography, with the maximum and average wear depths reaching about 70 µm. The volumetric parameters (Vvc = 5.84 mL/m^2 and Vvv = 0.259 mL/m^2) confirm extensive material loss and deep valley formation typical of abrasive micro-ploughing.

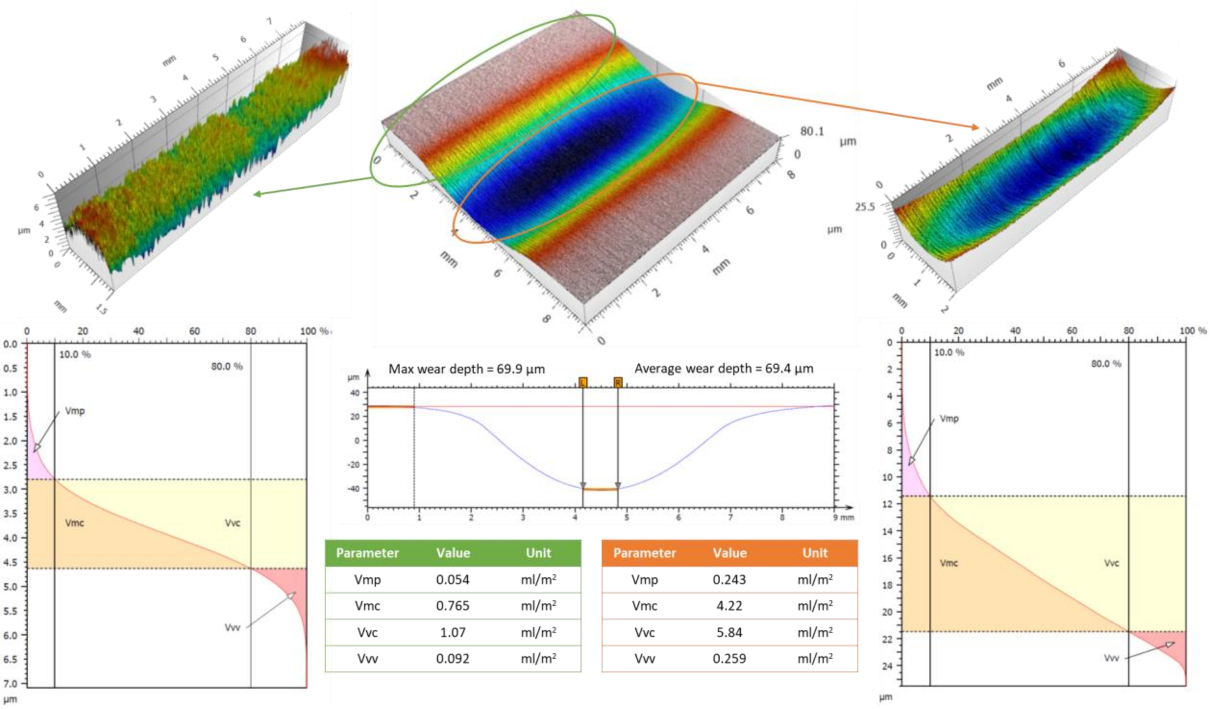

Parameter	Value	Unit
Vmp	0.054	ml/m²
Vmc	0.765	ml/m²
Vvc	1.07	ml/m²
Vvv	0.092	ml/m²

Parameter	Value	Unit
Vmp	0.243	ml/m²
Vmc	4.22	ml/m²
Vvc	5.84	ml/m²
Vvv	0.259	ml/m²

Figure 19. 3D isometric views, Abbott-Firestone curves, and volumetric parameters of their description for new (marked green) and worn (marked orange) surfaces of PA lubricated with the reference grease.

Under neat IL lubrication, both depth parameters decrease by nearly an order of magnitude (Max = 7.22 µm, Avg. = 7.14 µm), showing that IL forms a phosphate-rich tribochemical film that suppresses micro-cutting. The Abbott-Firestone curve becomes steeper in its central part, and the large reduction of Vmp (from 0.243 → 0.051 mL/m^2) together with a more moderate Vvv (0.259 → 0.196 mL/m^2) indicates that the IL primarily reduces peak deformation and wear initiation, though residual valleys remain.

For IL + CNTs 0.75 % wt., the wear track becomes markedly shallower (Max = 2.91 µm, Avg. = 2.86 µm), with Vvv decreasing to 0.104 mL/m^2 and Vmp increasing slightly compared with pure IL. This suggests that CNTs contribute to surface smoothing and partial reinforcement of the tribofilm, but the increased Vvc (2.67 mL/m^2) points to local inhomogeneities or incomplete consolidation of the carbonaceous layer.

The most favourable profile is obtained for IL + Ni-CNT 0.75 % wt., where the surface displays the lowest wear depths (Max = 2.70 µm; Avg. = 2.65 µm) and the most balanced volumetric characteristics (Vmp = 0.072, Vvc = 1.43, Vvv = 0.101 mL/m^2). The Abbott–Firestone curve reveals a compact core region and minimal valley fraction, indicating the formation of a continuous, load-supporting tribolayer. This Ni-assisted structure effectively stabilises the contact and limits both abrasive and adhesive wear mechanisms.

In summary, the progressive evolution of surface topography with lubricant formulation clearly demonstrates the synergistic effect of the ionic liquid and Ni-decorated CNTs. The IL ensures chemical surface passivation, while Ni-CNTs enhance the mechanical integrity and continuity of the tribofilm, producing the smoothest and most stable wear morphology.

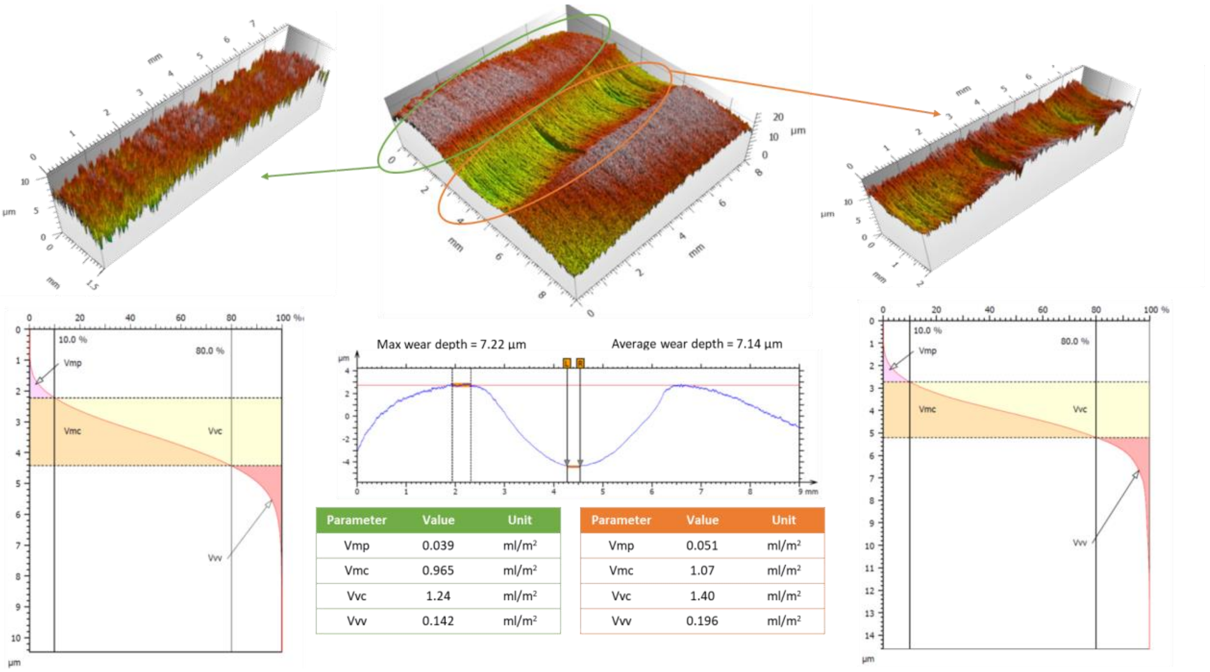

Parameter	Value	Unit
Vmp	0.039	ml/m²
Vmc	0.965	ml/m²
Vvc	1.24	ml/m²
Vvv	0.142	ml/m²

Parameter	Value	Unit
Vmp	0.051	ml/m²
Vmc	1.07	ml/m²
Vvc	1.40	ml/m²
Vvv	0.196	ml/m²

Fig. 20. 3D isometric views, Abbott-Firestone curves, and volumetric parameters of their description for new (marked green) and worn (marked orange) surfaces of PA lubricated with the neat IL.

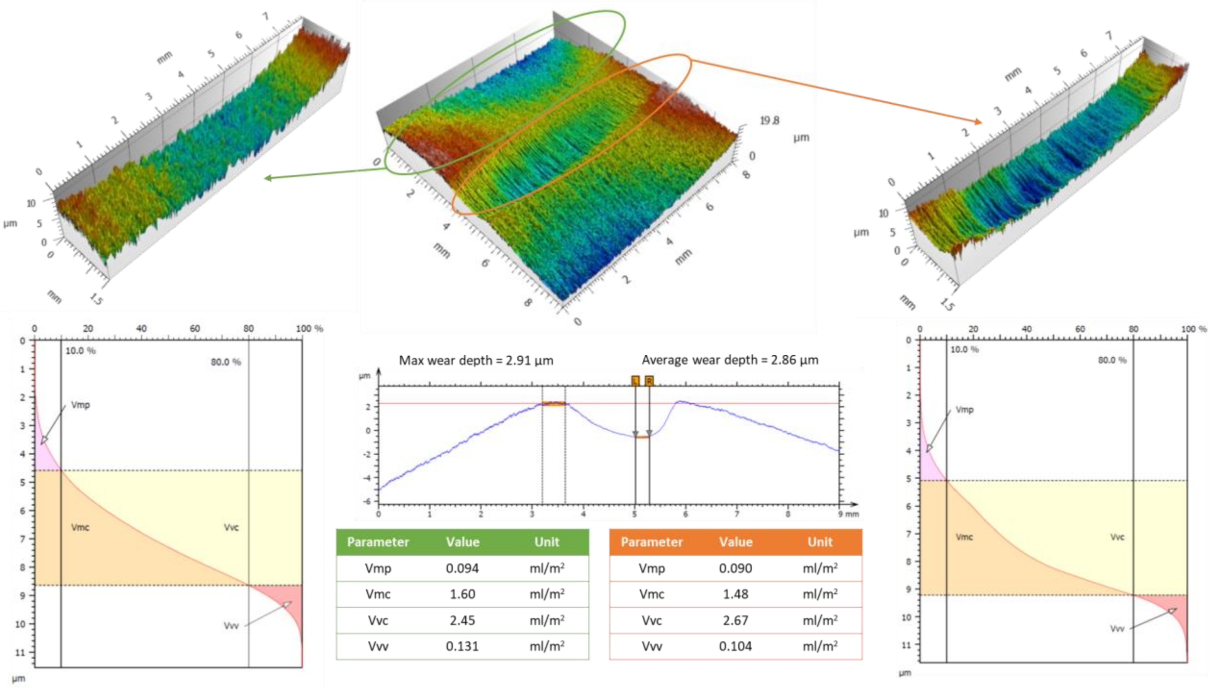

Parameter	Value	Unit
Vmp	0.094	ml/m²
Vmc	1.60	ml/m²
Vvc	2.45	ml/m²
Vvv	0.131	ml/m²

Parameter	Value	Unit
Vmp	0.090	ml/m²
Vmc	1.48	ml/m²
Vvc	2.67	ml/m²
Vvv	0.104	ml/m²

Figure 21. 3D isometric views, Abbott-Firestone curves, and volumetric parameters of their description for new (marked green) and worn (marked orange) surfaces of PA lubricated with IL + CNTs 0.75% wt.

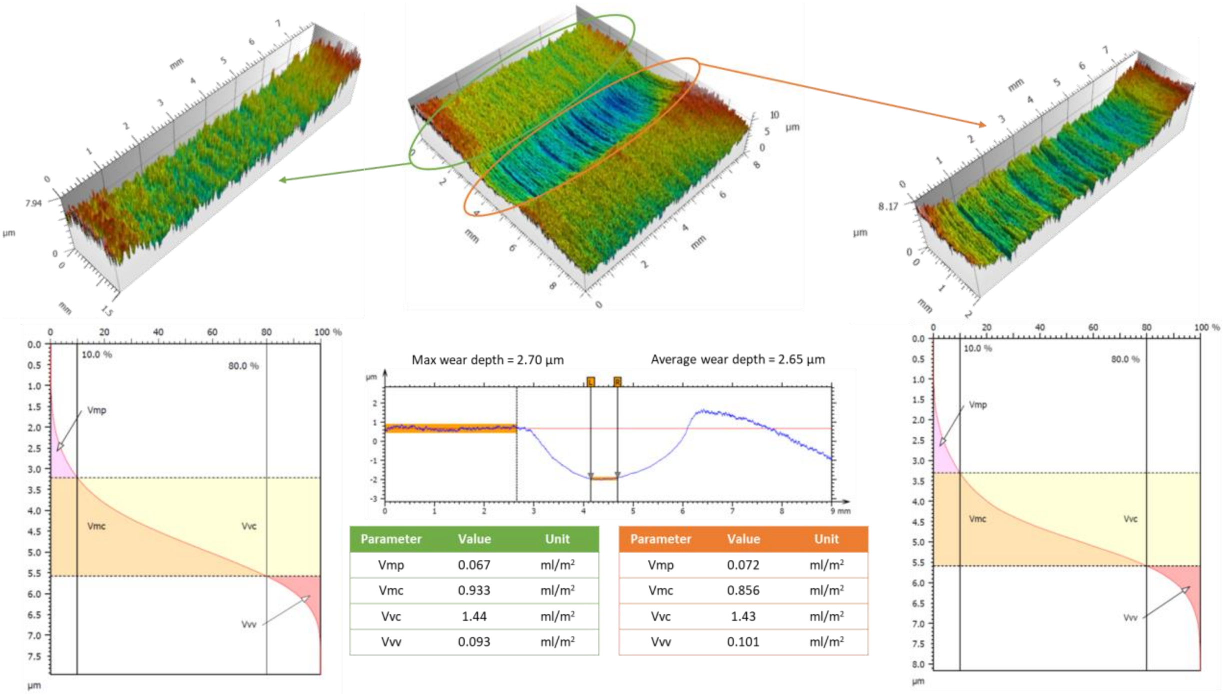

Parameter	Value	Unit
Vmp	0.067	ml/m²
Vmc	0.933	ml/m²
Vvc	1.44	ml/m²
Vvv	0.093	ml/m²

Parameter	Value	Unit
Vmp	0.072	ml/m²
Vmc	0.856	ml/m²
Vvc	1.43	ml/m²
Vvv	0.101	ml/m²

Figure 22. 3D isometric views, Abbott-Firestone curves, and volumetric parameters of their description for new (marked green) and worn (marked orange) surfaces of PA lubricated with IL + Ni-CNTs 0.75% wt.

The 2D surface profiles of wear tracks shown in Figures 19-22 reveal distinct differences in wear track morphology between the reference and IL-lubricated samples. In the reference case, the cross-section exhibits a smooth, open valley with no material accumulation along the edges, which is characteristic of abrasive wear dominated by debris ejection from the contact zone. In contrast, all IL-based lubricants – both neat and hybrid – exhibit clear edge pile-up ridges symmetrically located on both sides of the wear track. The height of these ridges reaches approximately 2-2.5 µm for neat IL and gradually decreases with the addition of CNTs and Ni-decorated CNTs.

This morphological feature is a strong indicator of the presence of a plastically deformable, tribo-chemically generated film that is laterally displaced during sliding rather than being completely removed. The ridge formation implies third-body retention and confinement of IL-derived material at the shear boundary, supporting the idea of a self-sustaining tribofilm acting as a dynamic reservoir of lubricant and debris. With the addition of CNTs, the pile-up becomes less pronounced and more asymmetric, suggesting that the solid phase reduces film flowability and introduces mild micro-ploughing effects.

The Ni-decorated CNTs further stabilise the tribofilm, yielding a shallower, smoother wear track with minimal pile-up. This indicates enhanced adhesion and structural coherence of the IL/Ni-CNT layer, which remains largely confined to the contact rather than being squeezed out. The absence of edge accumulation in the reference and its presence – followed by gradual reduction – in IL, IL + CNTs, and IL + Ni-CNTs lubricants, therefore, provides direct morphological evidence of progressive improvement in film integrity and load-bearing stability within the IL-based systems.

Figures 23-26 present the 3D surface topography maps of UHMWPE blocks after tests performed at 750 N, along with the corresponding AFCs and volumetric parameters extracted for the worn (orange) and unworn (green) regions.

The reference-lubricated UHMWPE sample (Figure 23) exhibits a broad, plastically deformed wear track with maximum and average depths of approximately 113 µm. The profile reveals pronounced material flow toward the track edges, forming gentle pile-ups rather than a purely open valley. The high valley-related parameters (Vvc = 6.54 mL/m², Vvv = 0.59 mL/m²) reflect deep subsurface deformation and incomplete material recovery typical of adhesive–plastic wear. The surface morphology indicates dominant viscoplastic displacement of the polymer, with limited fracture or detachment, consistent with the SEM-observed transfer film and adhesive junction remnants. The pronounced difference between Vmp and Vvv, therefore, reflects not only geometric displacement but also the absence of an effective tribochemical film capable of stabilising the contact under load.

Under neat IL lubrication, the UHMWPE surface (Figure 24) exhibits a shallower and more uniform wear track, with a maximum depth of ~64 µm. The wear track shows a smooth and continuous morphology, with delicate material pile-up along the edges but no signs of tearing or sharp ridges. This indicates the formation of a stable IL-derived tribochemical film that constrains polymer flow and limits adhesive junction formation. The reduced valley volumes (Vvc = 3.01 mL/m², Vvv = 0.32 mL/m²) confirm that IL effectively mitigates subsurface deformation and suppresses large-scale material displacement.

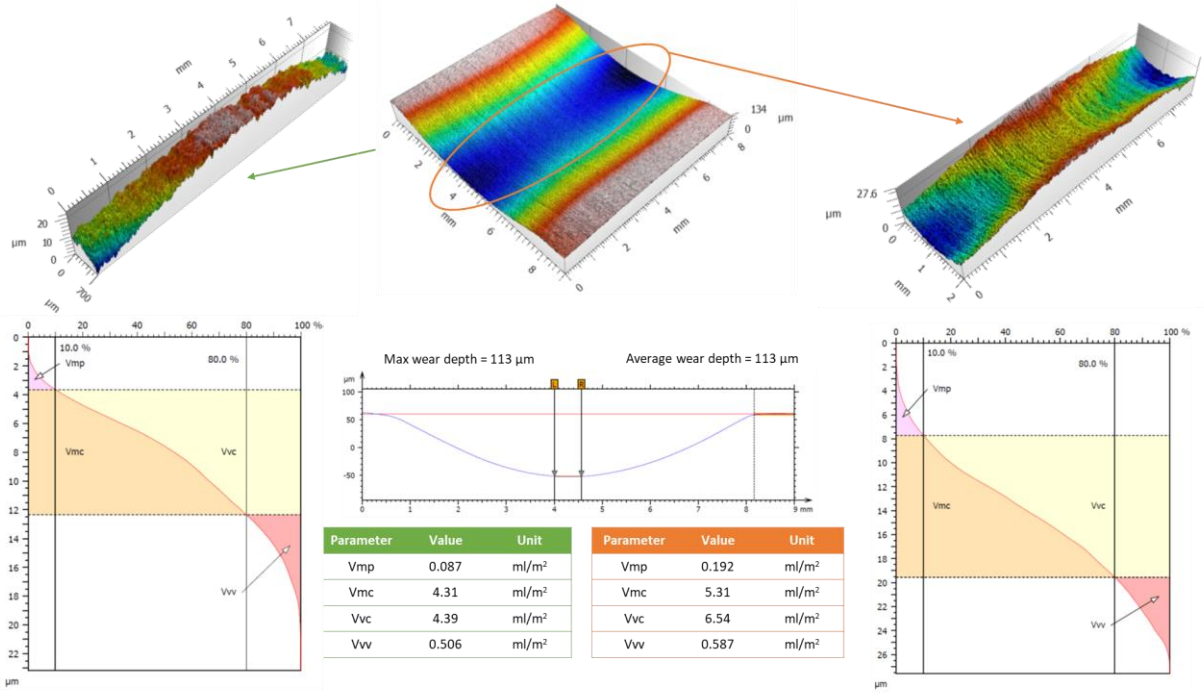

Parameter	Value	Unit
Vmp	0.087	ml/m^2
Vmc	4.31	ml/m^2
Vvc	4.39	ml/m^2
Vvv	0.506	ml/m^2

Parameter	Value	Unit
Vmp	0.192	ml/m^2
Vmc	5.31	ml/m^2
Vvc	6.54	ml/m^2
Vvv	0.587	ml/m^2

Figure 23. 3D isometric views, Abbott-Firestone curves, and volumetric parameters of their description for new (marked green) and worn (marked orange) surfaces of UHMWPE lubricated with the reference grease.

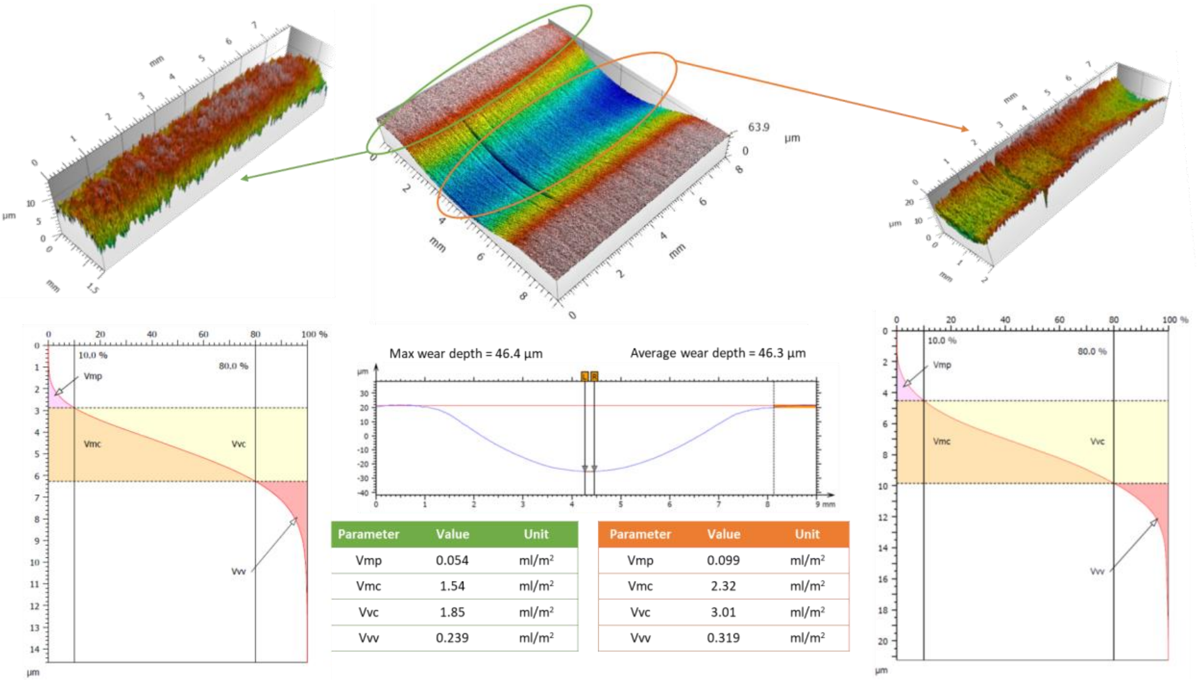

Parameter	Value	Unit
Vmp	0.054	ml/m^2
Vmc	1.54	ml/m^2
Vvc	1.85	ml/m^2
Vvv	0.239	ml/m^2

Parameter	Value	Unit
Vmp	0.099	ml/m^2
Vmc	2.32	ml/m^2
Vvc	3.01	ml/m^2
Vvv	0.319	ml/m^2

Figure 24. 3D isometric views, Abbott-Firestone curves, and volumetric parameters of their description for new (marked green) and worn (marked orange) surfaces of UHMWPE lubricated with the neat IL.

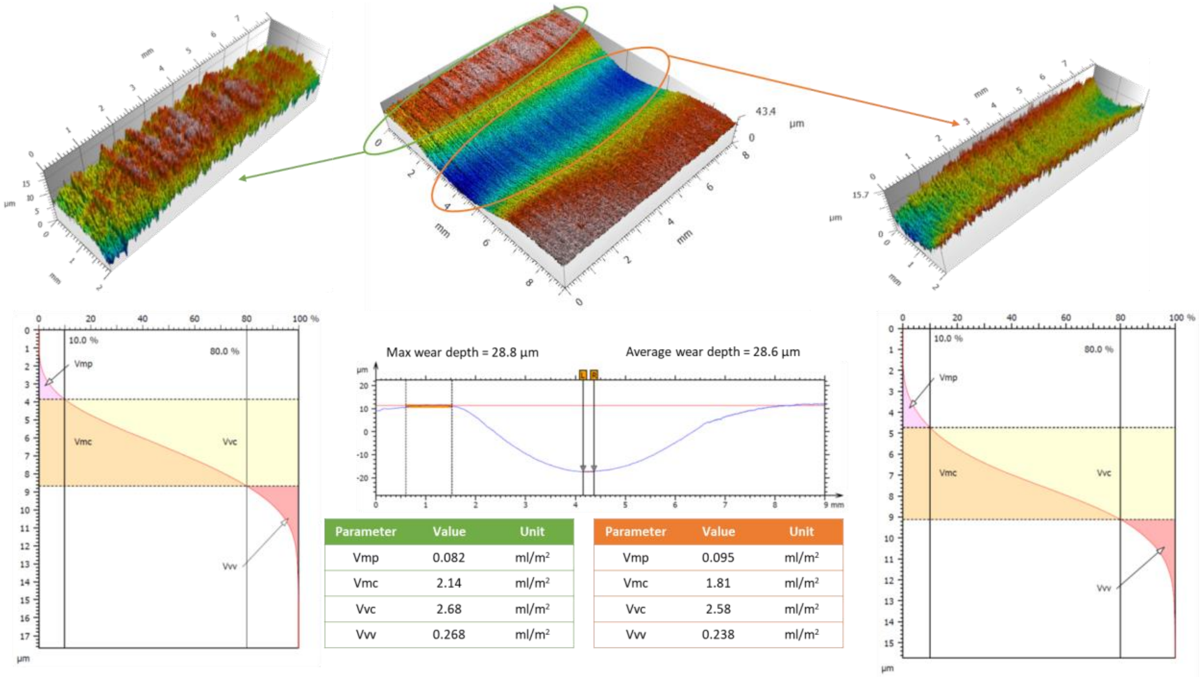

Parameter	Value	Unit
Vmp	0.082	ml/m²
Vmc	2.14	ml/m²
Vvc	2.68	ml/m²
Vvv	0.268	ml/m²

Parameter	Value	Unit
Vmp	0.095	ml/m²
Vmc	1.81	ml/m²
Vvc	2.58	ml/m²
Vvv	0.238	ml/m²

Figure 25. 3D isometric views, Abbott-Firestone curves, and volumetric parameters of their description for new (marked green) and worn (marked orange) surfaces of UHMWPE lubricated with IL + CNTs 0.75% wt.

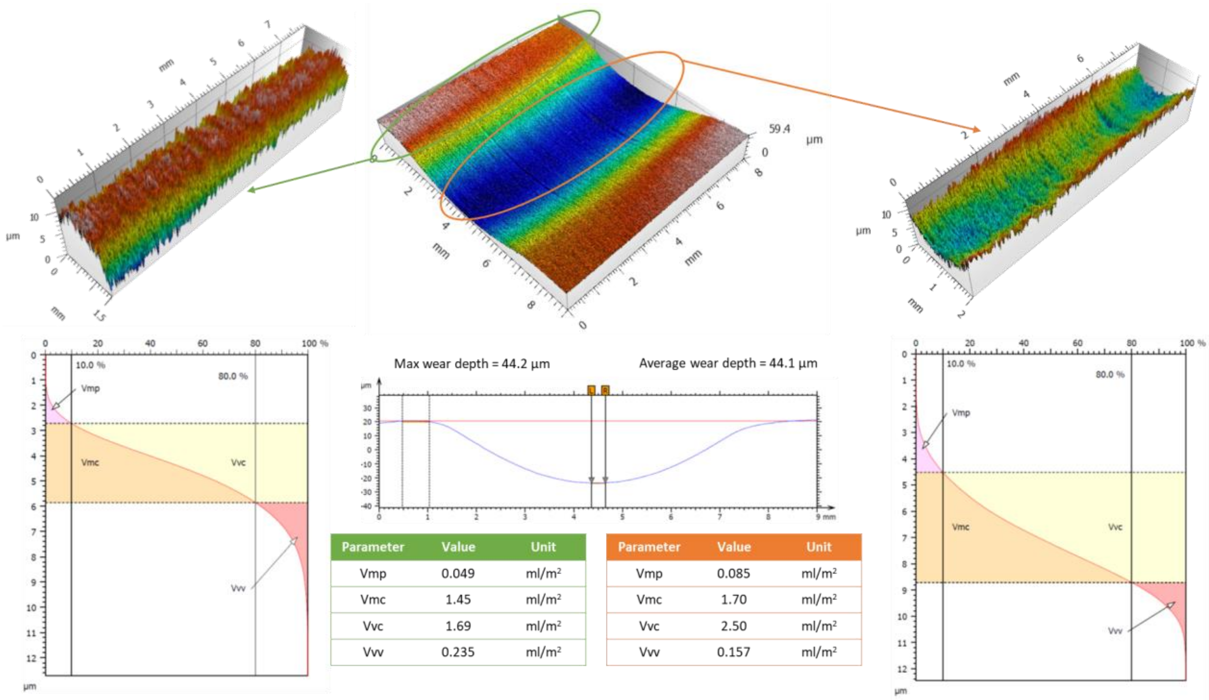

Parameter	Value	Unit
Vmp	0.049	ml/m²
Vmc	1.45	ml/m²
Vvc	1.69	ml/m²
Vvv	0.235	ml/m²

Parameter	Value	Unit
Vmp	0.085	ml/m²
Vmc	1.70	ml/m²
Vvc	2.50	ml/m²
Vvv	0.157	ml/m²

Figure 26. 3D isometric views, Abbott-Firestone curves, and volumetric parameters of their description for new (marked green) and worn (marked orange) surfaces of UHMWPE lubricated with IL + Ni-CNTs 0.75% wt.

In turn, lubrication with IL + CNT 0.75 % wt. (Figure 25) results in a further decrease in wear depth to ~44 µm (max 44.2 µm, avg 44.1 µm), with a relatively smooth floor and no pronounced edge pile-ups. The volumetric AFC parameters (Vmp = 0.085 mL/m², Vmc = 1.70 mL/m², Vvc = 2.50 mL/m², Vvv = 0.157 mL/m²) indicate moderate peak/core volumes and a reduced valley fraction compared with the reference and IL-lubricated surfaces. These features point to the formation of a compact and continuous boundary film reinforced by CNTs, effectively restricting plastic flow and stabilising the contact.

Finally, lubrication with IL + Ni-CNT 0.75 %wt. (Figure 26) produced a slightly deeper wear track than that observed for IL + CNT lubrication, despite comparable or even slightly lower volumetric parameters. This behaviour suggests that the overall material loss did not increase proportionally with track depth. The difference can be attributed to the distinct tribological role of nickel: while in stiffer polymers such as PA, Ni decoration promotes controlled CNT exfoliation and tribofilm formation, in the UHMWPE system, the nanotubes are embedded within the soft transfer layer, where Ni acts as a rigid inclusion rather than a tribochemical catalyst. This reduces local reactivity and may enhance plastic deformation, leading to a deeper but smooth and uniform track. The presence of Ni thus alters the balance between mechanical reinforcement and tribochemical protection, resulting in a compact yet less reactive boundary film.

The apparent divergence between friction and wear observed for UHMWPE can be explained by the distinct functional roles of the IL and CNT phases. The neat IL yielded the lowest COF because the interfacial shear occurred within a homogeneous, low-shear tribofilm dominated by IL. In contrast, the incorporation of CNTs (decorated or not) mainly improved the wear resistance by reinforcing the IL-derived and polymer transfer films. This structural strengthening reduced valley volumes (Vvc, Vvv) and suppressed plastic flow, but simultaneously increased the effective shear strength of the interface. The slightly higher polar component of surface free energy measured for CNT-containing tracks also suggests stronger interfacial adhesion, which may contribute to the moderate rise in COF [72,73]. Consequently, CNTs act primarily as anti-wear fillers rather than friction improvers in the UHMWPE-based contact, while the neat IL remains the most efficient anti-friction agent. Additionally, as UHMWPE represents more non-polar surface than PA [74], the wettability of the polymer surface and the corresponding adhesivity by the IL-based greases is higher for PA supporting formation of the stable interface upon friction.

4. Conclusions

Based on the presented results and their discussion, the following conclusions can be formulated:

- A new class of hybrid greases combining an ionic liquid (P_{66614} DEHP) with nickel-decorated CNTs was developed and successfully applied for lubricating metal-polymer friction pairs. The formulation demonstrated stable dispersion and satisfactory structural integrity of the Ni decoration, confirmed by TEM and EDX analyses.
- The hybrid greases substantially reduced friction compared with the commercial reference. For the PA-steel contact, the lowest COF (0.0168 at 750 N) was achieved with IL + Ni-CNTs 0.5 % wt., corresponding to a ~75 % friction reduction. For UHMWPE, the neat IL provided the most efficient antifriction performance, with COF values of 0.0178-0.0207 across the tested loads.
- SEM/EDS and Raman analyses revealed distinct wear mechanisms for the two polymers. In PA, Ni-CNTs promoted tribo-induced exfoliation of CNT walls and the formation of shear-adaptive carbonaceous films acting synergistically with IL-derived phosphate tribofilms. In UHMWPE, CNTs became embedded in the transfer layer, where Ni acted as a rigid inclusion rather than a tribochemical catalyst.
- Surface free energy studies confirmed that IL increased the polar character of both polymers through phosphate-based film formation, while Ni-CNTs slightly shifted the PA surface toward a more apolar, carbon-dominated state. In UHMWPE, CNTs remained inactive at the interface, preserving the IL-controlled chemical character.
- 3D surface topography confirmed the evolution from abrasive-plastic wear under reference grease to compact, load-supporting tribofilms under IL-based lubrication. The IL + CNTs and Ni-CNTs hybrids produced the smoothest and most consolidated wear tracks for PA, whereas in UHMWPE, the they mainly improved wear resistance rather than reducing friction.

5. Perspectives

The results demonstrate that combining ILs with metal-decorated carbon nanostructures offers a viable route toward new-generation hybrid greases with tuneable tribochemical and mechanical behaviour. Future work should focus on optimising the metal decoration concentration and particle distribution to enhance catalytic activity without compromising film stability. Expanding the concept to other metal-polymer systems and dynamic contact conditions may provide further insight into the load- and temperature-dependent mechanisms governing hybrid lubrication. Ultimately, the developed IL-Ni-CNT framework could serve as a model platform for designing environmentally adaptive, high-performance lubricants for lightweight mechanical systems and electric mobility applications.

Acknowledgement

The authors would like to acknowledge the financial support for this research provided by the National Science Centre in Poland (Project 2020/39/B/ST5/02562).

References

[1] Hirano M., Shinjo K., Superlubricity and frictional anisotropy, Wear, 1993, 168(1-2), pp. 121-125.

[2] Luo J., Zhou X., Superlubricitive engineering – Future industry nearly getting rid of wear and frictional energy consumption, Friction, 2020, 8(4), pp. 643-655.

[3] Zhneg Q., Zhang W., A systematic review of the recent advances in superlubricity research, Coatings, 2023, 13(12), 1989.

[4] Ayyagari A., Alam K.I., Berman D., Erdemir A., Progress in superlubricity across different media and material systems – a review, Frontiers in Mechanical Engineering, Sec. Tribology, 2022, 8.

[5] Baykara M.Z., Vazirisereshk M.R., Martini A., Emerging superlubricity: A review of the state of the art and perspectives on future research, Applied Physics Reviews, 2018, 5, 041102.

[6] Zhneg Z., Guo Z., Liu W., Luo J., Low friction of superslippery and superlubricity: A review, 2023, Friction, 11(7), pp. 1121-1137.

[7] Berman D., Deshmukh S.A., Sankaranarayanan S.K., Erdemir A., Sumant A.V., Macroscale superlubricity enabled by graphene nanoscroll formation, Science, 2015, 348(6239), pp. 1118-1122.

[8] Kim W.K., Falk M.L., Atomic-scale simulations on the sliding of incommensurate surfaces: The breakdown of superlubricity, Physical Review B, 2009, 80(23), 235428.

[9] Dienwiebel M., Verhoeven G.S, Pradeep N., Frenken J.W.M., Heimberg J.A., Zandbergen H.W., Physical Review Letters, 2004, 92(12), 126101.

[10] Shia P., Lua Y., Suna J., Tanga C., Wang Y., Jiang L., Qian L., Chen L., Towards a deeper understanding of superlubricity on graphite governed by interfacial adhesion, Carbon, 2022, 199, pp. 479-485.

[11] Buzio R., Gerbi A., Bernini C., Repetto L., Vanossi A., Graphite superlubricity enabled by triboinduced nanocontact, Carbon, 184, 2021, pp. 875-890.

[12] Fan S., Chen Y., Wu J., Xiao S., Chen G., Chu P.K., Structure, superlubricity, applications, and chemical vapor deposition methods of graphene solid lubricants, Tribology International, 2024, 198, 109896.

[13] Sang L.V., Sugimura N., Washizu H., Graphene as solid lubricant vertically buried into iron contact surface by annealing for superlubricity, Tribology International, 2022, 165, 107228.

[14] Huang P., Deng W., Qi W., Chen X., Tian J., Wang Y., Li X., Xu J., Zhang C., Luo J., Superlow friction and wear enabled by nanodiamond and hexagonal boron nitride on a-C:H films surfaces in dry nitrogen, Materials Today Nano, 2023, 24, 100384.

[15] Erdemir A., Eryilmaz O., Achieving superlubricity in DLC films by controlling bulk, surface, and tribochemistry, Friction, 2014 2(2), pp. 140-155.

[16] Erdemir A., Design criteria for superlubricity in carbon films and related microstructures, Tribology International, 2014, 37(7), pp. 577-583.

[17] Xing Z., Zhang J., Kaindl R., Zhang B., Solid superlubricity of diamond-like carbon f ilms: a review, Surface Science and Technology, 2025, 3, 16.

[18] Jang S., Chen Z., Kim S.H., Origin of superlubricity of diamond-like carbon (DLC), 2025, Friction 13(1), 9440995.

[19] Ky D.L.C., Tran Khac D.C., Le C.T., Kim Y.S., Chung K.H., Friction characteristics of mechanically exfoliated and CVD grown single-layer MoS_2, 2018, Friction, 6(4), 395-406.

[20] Shi Y., Zhang J., Pu J., Ren S., Wang H., Fan X., Ma T., Wang L., Robust macroscale superlubricity enabled by tribo-induced structure evolution of MoS_2/metal superlattice coating, Composites Part B, 2023, 250, 110460.

[21] Ma Q., Liang M., Xu X., Yan C., Wang H., Towards direct superlubricity and negligible wear with polyalcohol lubricant mixtures of ethylene glycol and glycerol for steel tribopairs, Applied Surface Science, 2024, 663, 160151.

[22] Fu X., Gou S., Wan Y., Zheng C., Li Q., Liu B., Superlubricity of TiN coating using glycerol with the addition of Cu nanoparticles, Tribology International, 2023, 181, 108327.

[23] Ma Q., He T., Khan A.M., Wang Q., Chung Y.W., Achieving macroscale liquid superlubricity using glycerol aqueous solutions, Tribology International, 2021, 160, 107006.

[24] Yang Y., Zhang R., Dong S., Ma X., Li J., Macroscopic superlubricity achieved by polyacrylic acid modified Fe_3O_4 nanoparticles as additives, Tribology International, 2024, 199, 110045.

[25] Du C., Yu T., Zhang L., Shen R., Wu Z., Li X., He X., Feng Y., Wang D., Robust and universal macroscale superlubricity with natural phytic acid solutions, Tribology International, 2023, 183, 108387.

[26] Gao Q., Hu J., Pei D., Li Z., Wang J., Yang S., Design and synthesis of boric acid-based deep eutectic solvents for green liquid superlubricity and bio-lubrication applications, Next Materials, 2025, 8, 100572.

[27] Li Z., Wang Y., Wang K., Jiang P., Zhang D., Superlubricity of ionic liquids at metal interfaces induced by tribochemical reactions, Applied Surface Science, 2025, 697, 162778.

[28] Chen H., Cai T., Li H., Ruan X., Jiao C., Atkin R., Wang Y., Gong P., Zhou X., Yu J., Jiang N., Macroscale superlubricity of steel by polymer-based ionic liquids without a running-in period, Tribology International, 2023, 182, 108349.

[29] Tang H., Chen X., Deng W., Luo J., Comprehensive review: Advances and critical mechanisms in liquid superlubricity, Advances in Colloid and Interface Science, 2025, 344, 103585.

[30] Wang K., Liu L., Liu Y., Luo J., Simple but effective: Liquid superlubricity with high load capacity achieved by ionic liquids, Materials Today Nano, 2022, 20, 100257.

[31] Wang K., Liu L., Song A., Ma T., Wang H., Luo J., Liu Y., Macroscale superlubricityunder ultrahigh contac pressure in the presence of layered double hydroxide nanosheets, Nano Research, 2022, 15(5), pp. 4700-4709.

[32] Wang W., Xie G., Luo J., Superlubricity of black phosphorus as lubricant additive, ACS Applied Materials & Interfaces, 2018, 10, pp. 43202-43210.

[33] Fu X., Guo S., Wan Y., Zheng C., Li Q., Liu B., Superlubricity of TiN coating using glycerol with the addition of Cu nanoparticles, Tribology International, 2023, 181, 108327.

[34] SunJ., Du S., Application of graphene derivatives and their nanocomposites in tribology and lubrication: a review, RSC Advances, 2019, 9, pp. 40642-40661.

[35] Opia A.C., Bin Abdollah M.F., Syahrullail S., Amiruddin H., Mamah C.S., Veza I., Effectiveness of carbon nanomaterials as lubricant additives: Recent review, Materials Today Nano, 2025, 30, 100643.

[36] Zhai W., Srikanth N., Kong L.B., Zhou K., Carbon nanomaterials in tribology, Carbon, 2017, pp. 150-171.

[37] Li J., Gao T., Luo J., Superlubricity of graphite induced by multiple transferred graphene nanoflakes, Advanced Science, 2018, 5(3), 1700616.

[38] Ge X., Chai Z., Shi Q., Liu Y., Wang W., Graphene superlubricity: A review, 2023, Friction, 11(11), pp. 1953-1973.

[39] Fu H., Yan G., Li M., Wang H., Chen Y., Yan C., Lin C.T., Jiang N., Yu J., Graphene as a nanofiller for enhancing the tribological properties and thermal conductivity of base grease, RSC Advances, 2019, 9, 42481.

[40] Liu Y., Ge X., Li J., Graphene lubrication, Applied Materials Today, 2020, 20, 100662.

[41] Renteria J.D., Nika D.L., Balandin A.A., Graphene thermal properties: applications in thermal management and energy storage, Applied Sciences, 2014, 4(4), pp. 525-547.

[42] Fuadi Z., Rahmadiawan D., Kurniawan R., Mulana F., Abral H., Nasruddin N., Khalid M., Effect of graphene nanoplatelets on tribological properties of bacterial cellulose/polyolester oil bio-lubricant, Frontiers in Mechanical Engineering, 2022, 8, 810847.

[43] Ye X., Songfeng E., Fan M., The influences of functionalized carbon nanotubes as lubricating additives: Length and diameter, Diamond & Related Materials, 2019, 100, 107548.

[44] Yu B., Liu Z., Zhou F., Liu W., Liang W., A novel lubricant additive based on carbon nanotubes for ionic liquids, Materials Letters, 2008, 62, pp. 2967–2969.

[45] Zhang Z., Yu G., Geng Z., Tian P., Ren K., Wu W., Gong Z., Ultra low friction of conductive carbon nanotube films and their structural evolution during sliding, Diamond & Related Materials, 2021, 120, 108617.

[46] Zhang S., Liu W.K., Ruoff R.S., Atomistic simulations of double-walled carbon nanotubes (DWCNTs) as rotational bearings, Nano Letters, 2004, 4(2), pp. 293-297.

[47] Nyholm N., Espallargas N., Functionalized carbon nanostructures as lubricant additives – A review, Carbon, 2023, 201, pp. 1200-1038.

[48] Reinert L., Lasserre F., Gachot C., Grützmacher P., MacLucas T., Souza N., Mücklich F., Suarez S., Long-lasting solid lubrication by CNT-coated patterned surfaces, Scientific Reports, 2017, 7, 42873.

[49] de Souza Lamim T., ,Martinez D.M., Pigosso T., Klein A.N., Bendo T., Binder C., Structural evolution of a carbon nanotube film under sliding wear: From a forest to a self-lubricating nanocomposite tribofilm, Carbon, 2025, 238, 120224.

[50] Wojciechowski Ł., Kubiak K.J., Boncel S., Marek A., Gapiński B., Runka T., Jędrysiak R., Ruszka S., Błaszkiewicz P. Mathia T.G., Tribology International, 2024, 191, 109203.

[51] Su Y., Tang Z., Wang G., Wan R., Influence of carbon nanotube on the tribological properties of vegetable based oil, Advances in Mechanical Engineering, 2018, 10(5), pp. 1-11.

[52] Lu W., Qiao X., Liu S., Chen P., A review of nanomaterials with different dimensions as lubricant additives, Nanomaterials, 2022, 12, 3780.

[53] Meng Y., Su F., Chen Y., Nickel/Multi-walled carbon nanotube nanocomposite synthesized in supercritical fluid as efficient lubricant additive for mineral oil, Tribology Letters, 2018, 66, 134.

[54] Skrzypek M., Wojciechowski Ł., Kałużny J., Boncel S., Marek A.A., Runka T., Nowicki M., Jędrysiak R., Ruczka S. Błaszkiewicz P., Carbon nanotubes decorated with nickel or copper as anti-wear and extreme-pressure additives for greases, Lubricants, 2024, 12(12), 448.

[55] Meng Y., Su F., Chen Y., Effective lubricant additive of nano-Ag/MWCNTs nanocomposite produced by supercritical CO_2 synthesis, Tribology International, 2018, 118, pp. 180-188.

[56] Wang J., Zhang H., Hu W., Li J., Tribological properties and lubrication mechanism of nickel nanoparticles as an additive in lithium grease, Nanomaterials, 2022, 12, 2287.

[57] Peng F., Fan S., Song N., Gao C., Zhang S., Zhang Y., Effect of nickel acetyl acetonate as lubricant additive in base oils with different molecular structure on in-situ formation and tribomechanism of carbon-based tribofilms of steel-steel sliding pair, Tribology Letters, 2024, 72, 56.

[58] Hernández Battez A., Bartolomé M., Blanco D., Viesca J.L., Fernández-González A., González R., Phosphonium cation-based ionic liquids as neat lubricants: Physicochemical and tribological performance, Tribology International, 2016, 95, pp.118-131.

[59] Barnhill W.C., Qu J., Luo H., Meyer III H.M., Ma Ch., Chi M., Papke B.L., Phosphonium-organophosphate ionic liquids as lubricant additives: Effects of cation structure on physicochemical and tribological characteristics, ACS Applied Materials & Interfaces, 2014, 6, pp. 21751-22928.

[60] ISO 25178-2:2021Geometrical product specifications (GPS) — Surface texture: Areal, Part 2: Terms, definitions and surface texture parameters.

[61] Owens D.K., Wendt R.C., Estimation of the surface free energy of polymers, Journal of Applied Polymer Science, 1969, 13, pp. 1741-1747.

[62] Stachowiak G.W., Batchelor A.W., Engineering tribology, 4th edition, Elsevier, 2014.

[63] Qiu Y., Hartwig J.F., Mechanism of Ni-catalyzed oxidations of unactivated $C(sp^3)$ – H bonds, Journal of the American Chemical Society, 2020, 142(45), 19239–19248.

[64] Kolanowska A., Wąsik P., Zięba W., Terzyk A.P., Boncel S., Selective carboxylation versus layer-by-layer unsheathing of multi-walled carbon nanotubes: new insights from the reaction with boiling nitrating mixture, RSC Advances, 2019, 9, 37608.

[65] Dzida M., Boncel S., Jóźwiak B., Greer H.F., Dulski M., Scheller Ł., Golba A., Flamholc F., Dzido G.,, Dziadosz J., Kolanowska A., Jędrysiak R., Blacha A., Cwynar K., Zorębski E., Bernardes C.E.S., Lourenço M.J.V., de Castro C.A.N., High-performance ionanofluids from subzipped carbon nanotube networks, ACS Applied Materials & Interfaces 2022 14 (45), 50836-50848.

[66] Ouyang Y., Cong L.M., Chen L., Liu Q.X., Fang Y., Raman study of single-walled carbon nanotubes and multi-walled carbon nanotubes with different laser excitation energies, Physica E: Low-dimensional Systems and Nanostructures, 2008, 40, 2386-2389.

[67] Runka T., Spectroscopic properties of polymer composites, Physical Sciences Reviews, 2017, 2(8), 20170025.

[68] Song Z., Yang Y., Hou P., Zhang X., Liang S., Wave absorbing properties of Ni Nanoparticle/CNT composite film fabricated by AAO/CNTs electrode, Helion, 2024, 10, e26054.

[69] Uematsu H., Kawasaki T., Koizumi K., Yamaguchi A., Sugihara S., Yamane M., Kawabe K., Ozaki Y., Tanoue S., Relationship between crystalline structure of polyamide 6 within carbon fibers and their mechanical properties studied using Micro-Raman spectroscopy, Polymer, 2021, 223, 123711.

[70] Bakshi S.R., Tercero J.E., Agarwal A., Synthesis and characterization of muliwalled carbon nanotube reinforced ultra-high molecular weight polyethylene composites by electrostatic spraying technique, Composites: Part A 38, 2007, 38, 2493-2499.

[71] Jin N., Song Y., Ma R., Li J., Li G., Zhang D., Characterization and identification of microplastics using Raman spectroscopy coupled with multivariate analysis, Analytica Chimica Acta, 2022, 1197, 339519.

[72] Wojciechowski Ł., Kubiak K.J., Mathia T.G., Impact of morphological furrows as lubricant reservoir on creation of oleophilic and oleophobic behaviour of metallic surfaces in scuffing, Tribology International, 2017, 116, 320-328.

[73] Wojciechowski Ł., Kubiak K.J., Mathia T.G., Roughness and wettability of surfaces in boundary lubricated scuffing wear, Tribology International, 2016, 93, Part B, 593-601.

[74] Sena J., Johannissen L.O., Blaker J.J., Hay S., A Machine learning lmodel for the prediction of water contact angles on solid polymers, The Journal of Physical Chemistry B, 2025, 129(10), 2739-2745.